AIAA JOURNAL
Vol. 49, No. 7, July 2011

Response of a Hypersonic Boundary Layer to Wall Blowing–Suction

Xiaowen Wang* and Xiaolin Zhong†
University of California, Los Angeles, Los Angeles, California 90095
and
Yanbao Ma‡
University of California, Merced, Merced, California 95343

DOI: 10.2514/1.J050173

In the laminar-turbulent transition of boundary-layer flows, the spatial development of boundary-layer waves, especially that of unstable waves, is important and indispensable. In this paper, the response of a Mach 8 flow over a 5.3° half-angle sharp wedge to wall blowing–suction is studied by numerical simulations. Steady base flow is obtained by solving the compressible Navier–Stokes equations with a combination of a fifth-order shock-fitting method and a second-order total-variation-diminishing scheme. In stability simulations, wall blowing–suction is introduced through an actuator on the wedge surface. The unsteady flow simulation is carried out using the shock-fitting method. The results show that mode F, mode S, acoustic waves, and entropy/vorticity waves are simultaneously excited by wall blowing–suction and coexist in the boundary layer just downstream of the actuator. For blowing–suction at a specific frequency, the results also show that mode S is strongly excited when the actuator is located upstream of the corresponding synchronization point. There is no significant amplification of pressure perturbation when the actuator is downstream of the synchronization point. This result represents a mixture of the receptivity and the downstream growth of mode S. The exact cause and mechanism of this result are not clear. However, such a result is obtained for wall blowing–suction at all frequencies considered in the current study. To excite a strong mode S at a specific frequency, the result indicates that it is necessary to place the blowing–suction actuator upstream of the corresponding synchronization point. Further theoretical analysis is needed to reveal the mechanism behind the numerical results.

I. Introduction

THE performances of hypersonic transportation vehicles and reentry vehicles are significantly affected by the laminar-turbulent transition of boundary-layer flows over vehicle surfaces, due to the fact that a turbulent boundary layer generates much higher drag and wall heat flux than a laminar one. Some success has been obtained in predicting heating rates in fully laminar or fully turbulent flows, but accurate predictions in a transitional regime remain elusive. Uncertainty in heat transfer rate requires large factors of safety to be used in current vehicle designs. Improved prediction of heat transfer rate and transition location could lead to significant improvements in hypersonic vehicle performance by allowing the removal of unnecessary weight in the thermal protection system.

Extensive studies have been carried out focusing on transition mechanisms [1,2]. The results show that the transition of a boundary-layer flow generally consists of the following three stages: receptivity, modal growth or transient growth, and breakdown to turbulence. Receptivity is the process during which environmental disturbances enter the boundary layer and excite the boundary-layer waves. For small-amplitude disturbance, modal growth of the unstable boundary-layer waves (which is linear and can be obtained by solving the eigenvalue problem of the homogeneous linearized stability equations) is important. With the disturbance amplitude increasing, transient growth (which is also linear and arises through the nonorthogonal nature of the Orr–Sommerfeld eigenfunctions and the Squire eigenfunctions) becomes important. Breakdown to turbulence is mainly caused by the nonlinear secondary instabilities when the boundary-layer waves reach certain amplitudes by means of modal growth or transient growth. Weak transient growth provides a higher initial amplitude for modal growth, whereas strong transient growth can lead to secondary instabilities and breakdown to turbulence right after the receptivity process (bypass transition).

No matter whether modal growth or transient growth has a larger contribution to the linear growth of the boundary-layer waves, study of the excitation and linear development of boundary-layer waves, especially for unstable waves, is important and indispensable because it provides initial conditions of amplitude, frequency, and phase angle for secondary instabilities and nonlinear breakdown. Fedorov and Khokhlov [3,4] theoretically studied the excitation of boundary-layer modes in supersonic and hypersonic boundary layers by acoustic waves. They found that acoustic waves can effectively excite both stable and unstable boundary-layer modes. Futhermore, stable modes played an important role in the excitation of unstable modes through intermodal exchange. Recently, Fedorov and Khokhlov [5] studied the receptivity of a hypersonic boundary layer over a flat plate to wall disturbances using a combination of asymptotic method and numerical calculation. In their research, different wall disturbances were considered, including wall vibrations, periodic blowing–suctions, and temperature disturbances. It was found that strong excitations of the boundary-layer waves occurred in local regions where forcing disturbances were resonant with the boundary-layer waves. Their theoretical results also showed that receptivity of the hypersonic boundary layer to blowing–suction is much stronger than that to wall vibrations and temperature disturbances. Tumin [6] calculated three-dimensional spatially growing perturbations in a two-dimensional compressible boundary layer. It was shown that within the scope of linearized Navier–Stokes equations, the perturbations could be presented as an expansion into a biorthogonal eigenfunction system. The results indicated that the

Presented as Paper 2005-5025 at the 35th AIAA Fluid Dynamics Conference and Exhibit, Toronto, Canada, 6–9 June 2005; received 1 September 2009; revision received 22 February 2011; accepted for publication 27 February 2011.

*Research Associate, Mechanical and Aerospace Engineering Department; xiaowen@seas.ucla.edu. Senior Member AIAA.
†Professor, Mechanical and Aerospace Engineering Department. Associate Fellow AIAA.
‡Assistant Professor, School of Engineering.

biorthogonal eigenfunction system could be used in the decomposition of flowfields obtained from direct numerical simulation (DNS) or experimental measurement, which was important for the quantitative studies on receptivity. For example, Tumin et al. [7] theoretically and numerically studied the receptivity of a hypersonic boundary layer over a sharp wedge to wall blowing–suction. The perturbation field downstream of the blowing–suction actuator was decomposed into the boundary-layer waves by using the biorthogonal eigenfunction system. It was found that there was good agreement between the normal mode amplitudes calculated with the help of the theoretical receptivity model and those obtained from projecting the numerical simulation results onto the normal modes.

Maslov and Semionov [8] experimentally studied the receptivity of a supersonic boundary layer to acoustic waves by using two parallel flat plates. The acoustic waves generated by an electric discharge system on the lower plate penetrated into the boundary layer of the upper plate as freestream disturbances. It was found that acoustic waves were converted into the boundary-layer waves most efficiently at the leading edge, in the neighborhood of the acoustic branch of the neutral curve, and in the vicinity of the lower branch of the neutral curve. A similar experiment was carried out for a Mach 5.92 flat-plate boundary layer by Maslov et al. [9] to study the leading-edge receptivity. They found that Tollmien–Schlichting waves were generated by acoustic waves impinging on the leading edge. The results also showed that the receptivity coefficients depended on wave inclination angles. Fedorov [10] investigated the receptivity of a high-speed boundary layer to acoustic disturbances using a combined numerical and asymptotic approach. The leading-edge receptivity problem of Maslov et al. [9] was studied, focusing on physical mechanisms associated with the diffraction and scattering of the acoustic waves. Their theoretical predictions of receptivity coefficient had good agreement with the experimental data. Semionov and Kosinov [11] studied the leading-edge receptivity of a supersonic boundary layer over a blunted flat plate to controlled disturbances. Their experimental setup was quite similar to that of Maslov et al. [9]. The controlled disturbances were excited by an electric discharge system. Their results showed that the boundary-layer waves excited by externally controlled disturbances at the blunted leading edge were stronger than those at the sharp leading edge. Wheaton et al. [12] measured instability and transition in the Boeing/AFOSR Mach-6 Quiet Tunnel. They designed a flared cone with a constant-thickness boundary layer to obtain a larger N factor of Mack's second mode under quiet flow conditions. It was found that the boundary layer remained laminar when large instability waves with the N factor of 13 and above were measured. Transition was observed only under noisy conditions, where the boundary-layer waves were less visible.

With the development of high-performance computers and numerical techniques, DNS has been a powerful tool to study boundary-layer transition problems. By solving the compressible linearized Navier–Stokes equations, Malik et al. [13] investigated the responses of a Mach 8 flow over a sharp wedge to three types of external forcing: a planar freestream acoustic wave, a narrow acoustic beam enforced on the bow shock near the leading edge, and a blowing–suction slot on the wedge surface. They concluded that these three types of forcing eventually resulted in the same type of instability waves in the boundary layer. Zhong [14] studied the receptivity of a hypersonic flow over a parabola to freestream disturbances by solving full Navier–Stokes equations. It was concluded that the generation of boundary-layer waves was mainly because of the interaction of the boundary layer with the transmitted acoustic waves. Compared with acoustic waves, entropy/vorticity waves were weaker in boundary-layer wave excitation. Ma and Zhong [15] studied the receptivity mechanism of a supersonic boundary layer to various freestream disturbances. They found that, in addition to the conventional Mack's first and second modes, there existed a family of stable waves (mode F) that played an important role in the excitation of the unstable waves. Such results were consistent with the theoretical analysis of Fedorov and Khokhlov [3,4]. Egorov et al. [16] numerically solved unsteady two-dimensional flows relevant to the receptivity of the supersonic and hypersonic boundary layers using a second-order total-variation-diminishing (TVD) scheme. To compare with numerical simulation results, theoretical analyses were carried out by the conventional linear stability theory (LST) and the LST including nonparallel flow effects. It was noted that nonparallel flow effects stabilized Mack's second mode. For small-amplitude forcing, the growth rate of Mack's second mode obtained from numerical simulation had good agreement with those predicted by the LST including nonparallel flow effects. Egorov et al. [17] also studied the unsteady two-dimensional flow relevant to the stability of a Mach 6 flat-plate boundary layer. It was found that for small-amplitude blowing–suction, the growth rate of Mack's second mode computed by DNS agreed well with those predicted by the LST including nonparallel flow effects.

Recently, Zhong and Ma [18] numerically studied the receptivity to weak-freestream fast acoustic waves for a Mach 7.99 axisymmetric flow over a 7° half-angle blunt cone. They found that no Mack's first mode was excited by freestream fast acoustic waves in the early region along the cone surface. In this case, the excitation of Mack's second mode was because of a two-step resonant process, i.e., the resonant between fast acoustic waves and mode F near the leading edge and the resonant between mode F and mode S. The two-step receptivity scenario observed from numerical simulations was consistent with that described by Fedorov and Khokhlov [19]. Maslov et al. [20] studied the evolution of disturbances in a Mach 21 flat-plate boundary layer by solving the unsteady Navier–Stokes equations with a high-order shock-capturing scheme. The numerical results were agree well with the data obtained from the locally parallel linear stability theory and experimental measurements in a hypersonic wind tunnel. Malik and Balakumar [21] investigated the receptivity of a Mach 4.5 flow over a flat plate to slow and fast acoustic waves. The results showed that the boundary layer was much more receptive to slow acoustic waves than to fast acoustic waves. The effect of the leading-edge thickness was also considered by numerical simulations. It was found that bluntness tended to stabilize the boundary layer. These results were consistent with the theoretical analyses of Fedorov [10] and the numerical results of Egorov et al. [16,17]. Wang and Zhong [22] numerically investigated the steady base flow and the receptivity of the hypersonic boundary layer corresponding to Maslov et al.'s [9] leading-edge receptivity experiments. The accuracy of the numerical simulation was validated by comparisons with the experimental measurements of Maslov et al. and the theoretical self-similar boundary-layer solution. A model of wall perturbation is proposed based on physical properties of the electric pulse generator used in the experiments of Maslov et al. [9] and Semionov and Kosinov [11]. Numerical results indicated that receptivity mechanism of the hypersonic boundary layer to wall perturbation was independent of the specific perturbation type. On the other hand, the hypersonic boundary layer was found to be most sensitive to blowing–suction and least sensitive to temperature perturbation. Additional research on the receptivity and stability of hypersonic boundary layers can be found in the review paper of Saric et al. [2].

Up to now, receptivity studies have focused more on freestream disturbances than on wall disturbances. However, the receptivity to wall disturbances, including blowing–suction, is also important. Wall disturbances, together with freestream disturbances, are the main disturbances that hypersonic vehicles experience under the real flight conditions. Blowing–suction is not only the most sensitive wall disturbance for hypersonic boundary layers, but is also widely used to control the boundary-layer transition. For example, Egorov et al. [23] studied the effect of porous coating on the stability and receptivity of a Mach 6 flat-plate boundary layer. In their numerical simulations, porous coating was modeled by pressure-perturbation-related wall blowing–suction.

In this paper, the response of a Mach 8 flow over a 5.3° half-angle sharp wedge to wall blowing–suction is studied. The flow conditions are the same as those of Malik et al. [13]. The steady base flow is obtained by solving the compressible Navier–Stokes equations with a combination of a fifth-order shock-fitting method and a second-order TVD scheme. In stability simulations, wall blowing–suction is introduced through an actuator on the wedge. The unsteady

flow simulation is carried out using the fifth-order shock-fitting method to achieve high-order accuracy. Stability characteristics of the boundary-layer waves are evaluated by the conventional LST. Seven cases of unsteady simulations are considered with the actuator shifting along the wedge surface to study the effect of the actuator location. The objective of this paper is to present and analyze numerical results, especially focusing on the effect of the actuator location.

Figure 1 shows a schematic of the response of a hypersonic boundary layer over a sharp wedge to wall blowing–suction. When wall blowing–suction is introduced on the wedge surface downstream of the leading edge, boundary-layer waves are excited and propagate downstream. The induced acoustic waves also radiate into the flow outside the boundary layer and interact with the bow shock. The waves' excitation and propagation in the boundary layer, as well as their interaction with the bow shock, are accurately captured by the fifth-order shock-fitting method.

II. Governing Equations and Numerical Methods

In the current study, a Mach 8 flow over a sharp wedge is considered, as shown in Fig. 1. The flow is assumed to be thermally and calorically perfect. The governing equations for numerical simulation are the compressible Navier–Stokes equations in the conservative form, i.e.,

$$\frac{\partial \mathbf{U}^*}{\partial t^*} + \frac{\partial(\mathbf{F}^*_{1i} + \mathbf{F}^*_{1v})}{\partial x^*_1} + \frac{\partial(\mathbf{F}^*_{2i} + \mathbf{F}^*_{2v})}{\partial x^*_2} = 0 \tag{1}$$

where the superscript $*$ represents dimensional variables. The vector $\mathbf{U}^*$ contains the conservative variables of mass, momentum, and energy, i.e.,

$$\mathbf{U}^* = \{\rho^*, \rho^* u^*_1, \rho^* u^*_2, e^*\} \tag{2}$$

The flux vector in Eq. (1) is divided into its inviscid and viscous components, because the two components are discretized with different finite difference schemes. The components $\mathbf{F}^*_{1i}$ and $\mathbf{F}^*_{2i}$ are inviscid flux vectors, whereas $\mathbf{F}^*_{1v}$ and $\mathbf{F}^*_{2v}$ are viscous flux vectors. The flux vectors are expressed as

$$\mathbf{F}^*_{ji} = \begin{bmatrix} \rho^* u^*_j \\ \rho^* u^*_1 u^*_j + p^* \delta_{1j} \\ \rho^* u^*_2 u^*_j + p^* \delta_{2j} \\ u^*_j (e^* + p^*) \end{bmatrix}$$

$$\mathbf{F}^*_{jv} = \begin{bmatrix} 0 \\ -\tau^*_{1j} \\ -\tau^*_{2j} \\ -\tau^*_{1j} u^*_1 - \tau^*_{2j} u^*_2 - k^* \frac{\partial T^*}{\partial x^*_j} \end{bmatrix} \tag{3}$$

with $j \in \{1, 2\}$. For perfect gas, pressure and energy are given by

$$p^* = \rho^* R^* T^* \tag{4}$$

$$e^* = \rho^* c^*_v T^* + \frac{\rho^*}{2}(u^{*2}_1 + u^{*2}_2) \tag{5}$$

where c^*_v is the specific heat at constant volume. For a compressible Newtonian flow, the viscous stress tensor is written as

$$\tau^*_{ij} = \mu^* \left(\frac{\partial u^*_i}{\partial x^*_j} + \frac{\partial u^*_j}{\partial x^*_i} \right) - \frac{2}{3} \mu^* \left(\frac{\partial u^*_1}{\partial x^*_1} + \frac{\partial u^*_2}{\partial x^*_2} \right) \delta_{ij} \tag{6}$$

with $i, j \in \{1, 2\}$. In the simulation, the viscosity μ^* and the heat conductivity k^* in Eq. (3) are calculated using Sutherland's law, together with a constant Prandtl number Pr. They are both functions of temperature only, i.e.,

$$\mu^* = \mu^*_r \left(\frac{T^*}{T^*_r} \right)^{3/2} \frac{T^*_r + T^*_s}{T^* + T^*_s} \tag{7}$$

$$k^* = \frac{\mu^* c^*_p}{Pr} \tag{8}$$

where $\mu^*_r = 1.7894 \times 10^{-5}$ Ns/m^2, $T^*_r = 288.0$ K, $T^*_s = 110.33$ K, and c^*_p is the specific heat at constant pressure. In this paper, the dimensional variables are scaled by freestream parameters. Specifically, density ρ^*, temperature T^*, velocities u^*_1 and u^*_2, and pressure p^* are scaled by ρ^*_∞, T^*_∞, u^*_∞, and $\rho^*_\infty u^{*2}_\infty$. Furthermore, x^*_1 is scaled by the unit length in meter, whereas x^*_2 is scaled by $\sqrt{\mu^*_\infty x^*_1 / \rho^*_\infty u^*_\infty}$.

The high-order shock-fitting method of Zhong [24] is used to solve the governing equations in a domain bounded by the bow shock and the wedge surface. The bow shock is treated as a boundary of the computational domain, which makes it possible for the governing equations to be spatially discretized by high-order finite difference methods. Specifically, a fifth-order upwind scheme is used to discretize the inviscid flux derivatives, whereas a sixth-order central scheme is used to discretize the viscous flux derivatives. The position and velocity of the shock front are treated as two unknown flow variables, computed by solving two additional equations:

$$\begin{cases} \frac{\partial H_\tau}{\partial \tau} = f\left(\xi, \zeta, \mathbf{U}_p, \mathbf{I}_N \cdot \left(\frac{\partial \mathbf{U}}{\partial \tau} \right)_p, \mathbf{U}_\infty, \frac{\partial \mathbf{U}_\infty}{\partial \tau}, H, H_\tau \right) \\ \frac{\partial H}{\partial \tau} = H_\tau \end{cases} \tag{9}$$

where H and H_τ are the position and velocity of the shock front, respectively. The subscripts p and ∞ represent flow variables on the high-pressure and freestream sides of the shock. The quantity $\mathbf{I}_N$ is the left eigenvector corresponding to the maximum eigenvalue. The above two equations are derived from the combination of the Rankine–Hugoniot relation across the shock and a characteristic compatibility relation from the downstream flowfield. Once H and H_τ are solved, the flow variables behind the shock can be computed using the jump conditions. Temporal integration of the governing equations, including the two equations for the shock front, is calculated using a Runge–Kutta method. More details of the high-order shock-fitting method can be found in Zhong's paper [24].

In the leading-edge region, there exists a singular point at the tip of the wedge (no definition of the position of the shock front). Therefore, the computational domain for the fifth-order shock-fitting method starts at $s^* = 0.00409$ m and ends at $s^* = 1.48784$ m, corresponding to $R = 182.7$ and 3485.4, respectively. In actual simulations, the computational domain is divided into 30 zones with a total of 5936 grid points in the streamwise direction and 121 grid points in the wall-normal direction. Forty-one grid points are used in the overlap region between two neighboring zones, which is sufficient to make the solution accurate and smooth within the whole domain. An exponential stretching function is used in the wall-normal direction to cluster more points inside the boundary layer. The spatial convergence of numerical simulation results based on this grid structure has been evaluated by grid refinement studies [7]. For the first zone of the shock-fitting calculations, inlet conditions are obtained from the solution of a second-order TVD scheme, which is used to solve the steady base flow in a small region including the leading edge. For other zones, inlet conditions are interpolated from the solution of the previous zone. The inlet conditions consist of the five conservative variables. For unsteady simulation, blowing–suction disturbances are introduced in a downstream region where the shock-fitting method is used. Compared with hybrid numerical methods that generally combine a high-order method in smooth regions and a shock-capturing method near the shock, the shock-fitting method can achieve uniform fifth-order accuracy in the whole domain, even at the shock front. By using the shock-fitting method, the interaction between the bow shock and unsteady disturbances is fully considered.

Because of the symmetric geometry, only the flowfield over the upper surface of the sharp wedge is simulated. As shown in Fig. 1,

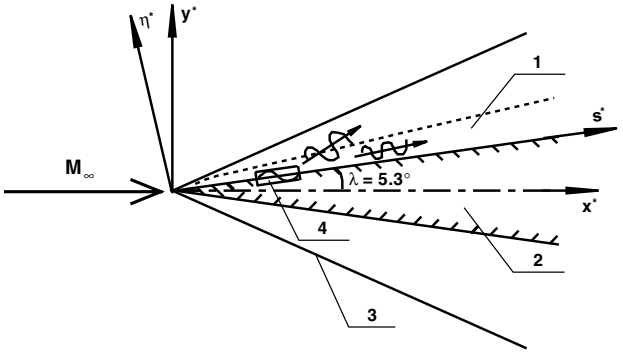

Fig. 1 Schematic of the response of a hypersonic boundary layer over a sharp wedge to wall blowing–suction; 1: boundary layer, 2: sharp wedge, 3: bow shock, and 4: blowing–suction actuator.

two Cartesian coordinate systems are used simultaneously to plot the results more conveniently. The coordinate s^* is defined as the distance along the wedge surface measured from the leading edge, and the coordinate η^* is the normal distance from the wall. The transformation between the two coordinate systems is as follows:

$$\begin{cases} s^* = x^* \cos\lambda + y^* \sin\lambda \\ \eta^* = -x^* \sin\lambda + y^* \cos\lambda \end{cases} \tag{10}$$

where λ is the wedge half-angle. The coordinate s^* can be converted to the local Reynolds number Re_s by

$$Re_s = Re^*_\infty s^* \tag{11}$$

where Re^*_∞ is the unit Reynolds number defined as

$$Re^*_\infty = \frac{\rho^*_\infty u^*_\infty}{\mu^*_\infty} \tag{12}$$

In the studies of boundary-layer stability, the Reynolds number based on the length scale of the local boundary-layer thickness, L^*, is generally used. They are expressed as

$$R = \frac{\rho^*_\infty u^*_\infty L^*}{\mu^*_\infty} \tag{13}$$

$$L^* = \sqrt{\frac{\mu^*_\infty s^*}{\rho^*_\infty u^*_\infty}} \tag{14}$$

Hence, the relation between R and Re_s is given by

$$R = \sqrt{Re_s} \tag{15}$$

III. Flow Conditions and Blowing–Suction Model

The freestream flow conditions of the hypersonic boundary layer over the sharp wedge of a 5.3° half-angle are as follows:

$M_\infty = 8.0$, $T^*_\infty = 54.78$ K, $p^*_\infty = 389$ Pa,

$Pr = 0.72$, $Re^*_\infty = 8.2 \times 10^6/\text{m}$,

Total length of the wedge surface ≈ 1.5 m

For the simulation of steady base flow, the wall is adiabatic, and the boundary condition of velocities on the wedge surface is the no-slip condition. When high-frequency blowing–suction disturbances are introduced to the steady base flow, isothermal condition is applied on the wall for unsteady simulation. This temperature condition is a standard boundary condition for theoretical and numerical studies on the boundary-layer stabilities. For example, the isothermal condition has also been used by Egorov et al. [23]. Meanwhile, the no-slip condition is applied on the wall, except in the blowing–suction region. Inlet conditions are specified. A fourth-order extrapolation is used for outlet conditions, because the flow is supersonic at the exit, except a small region close to the wedge surface. A buffer region, including 41 grid points in the streamwise direction, is used to take into account the effect of the subsonic region.

In Fedorov and Khokhlov's [5] theoretical and numerical analyses on the receptivity of a hypersonic boundary layer to wall disturbances, wall blowing–suction has the following traveling-wave form:

$$\begin{bmatrix} u' \\ v' \\ w' \\ \theta' \end{bmatrix} = g(x) \begin{bmatrix} 0 \\ 1 \\ 0 \\ 0 \end{bmatrix} \exp(i\alpha_c x + i\beta_c z - i\omega t) \tag{16}$$

where u', v', and w' are velocity disturbances in the streamwise, wall-normal, and spanwise directions; θ' is the temperature disturbance; the parameters α_c and β_c are wave number components in the streamwise and spanwise directions; ω is the circular frequency; and the function $g(x)$ represents the disturbance profile. Equation (16) implies that wall blowing–suction is only related to the wall-normal velocity disturbance. For this model, small instantaneous mass flux is generally introduced to the boundary layer.

Another model of blowing–suction is to impose mass flux oscillations on the wall, which has been used by Eibler and Bestek [25]. According to this model, wall blowing–suction has the following form:

$$\frac{\rho_w v_w}{\rho_\infty u_\infty} = Q \sin\left(2\pi \frac{x - x_1}{x_2 - x_1}\right) \sin\omega t \tag{17}$$

where Q is the amplitude of mass flux oscillation, $\rho_w v_w$ is the local mass flux oscillation in the wall-normal direction, and $\rho_\infty u_\infty$ is the freestream mass flux in the streamwise direction. The coordinates x_1 and x_2 represent the leading and trailing edges of the blowing–suction region. Because of the antisymmetric profile of the sine function within the forcing region, no instantaneous mass flux is introduced to the boundary layer.

In the current study, a blowing–suction model similar to Eq. (17) is used. Mass flux oscillations on the wedge surface within the forcing region are written as

$$(\rho^* v^*)' = q^*_0 \epsilon \beta(l) \sum_{n=1}^{15} \sin \omega^*_n t^* \tag{18}$$

where q^*_0 is an amplitude constant depending on the location of the actuator, and ϵ is a small dimensionless parameter. The function $\beta(l)$ is the profile function defined as

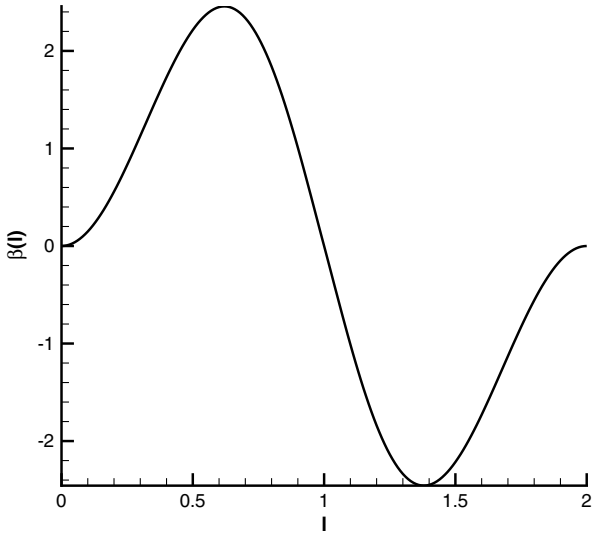

Fig. 2 Profile of the blowing–suction disturbances in the forcing region.

$$\beta(l) = \begin{cases} 20.25l^5 - 35.4375l^4 + 15.1875l^2 & \text{if } 0 \le l \le 1 \\ -20.25(2-l)^5 + 35.4375(2-l)^4 - 15.1875(2-l)^2 & \text{if } 1 \le l \le 2 \end{cases} \tag{19}$$

The variable l is a dimensionless coordinate defined within the forcing region:

$$l = \frac{2(s^* - s_i^*)}{s_e^* - s_i^*} \tag{20}$$

where s_i^* and s_e^* are the coordinates of the leading and trailing edges of the actuator. Figure 2 shows the profile of the blowing–suction disturbances in the forcing region. Because of the antisymmetric property of the fifth-order polynomial profile function within the blowing–suction region, no instantaneous mass flux is introduced to the boundary layer. Compared with the sine function in Eq. (17), the current profile function makes smoother the mass flux oscillations at the edges of the actuator. In Eq. (18), ω_n^* stands for the circular frequency ($n = 1, 2, \ldots, 15$), which is related to the frequency by

$$\omega_n^* = 2\pi f_n^* = 2\pi n f_1^* \qquad (n = 1, 2, \ldots, 15) \tag{21}$$

The circular frequency ω_n^* and the frequency f_n^* are scaled as follows:

$$\omega_n = \frac{\omega_n^* L^*}{u_\infty^*} \tag{22}$$

$$F_n = \frac{2\pi f_n^* \mu_\infty^*}{\rho_\infty^* u_\infty^{*2}} = \frac{\omega_n^* \mu_\infty^*}{\rho_\infty^* u_\infty^{*2}} \tag{23}$$

With the definitions of the Reynolds number R and the dimensionless frequency F_n, the dimensionless circular frequency can also be expressed as

$$\omega_n = RF_n \tag{24}$$

The dimensionless parameter ϵ in Eq. (18) is assigned the following value:

$$\epsilon = 1.0 \times 10^{-5} \tag{25}$$

which is small enough to preserve linear properties of the disturbances. The frequency f_n^*, dimensionless circular frequency ω_n, and dimensionless frequency F_n for the 15-frequency blowing–suction disturbances are listed in Table 1.

Table 1 Frequency, dimensionless circular frequency, dimensionless frequency, locations of the synchronization point and branch II neutral point for the 15-frequency blowing–suction disturbances

n	f_n^*, kHz	ω_n^*, kHz	$F_n \times 10^6$	s_{sn}^*, m	R_{sn}	$s_{\mathrm{II}n}^*$, m
1	14.92	93.74	9.63	16.9885	11882.658	68.38297
2	29.84	187.48	19.26	4.2471	5941.329	17.09574
3	44.76	281.23	28.89	1.8876	3960.886	7.59811
4	59.68	374.97	38.52	1.0618	2970.664	4.27394
5	74.60	468.71	48.15	0.6795	2376.532	2.73532
6	89.52	562.45	57.78	0.4719	1980.443	1.89953
7	104.44	656.19	67.41	0.3467	1697.523	1.39557
8	119.36	749.94	77.04	0.2654	1485.332	1.06848
9	134.28	843.68	86.67	0.2097	1320.295	0.84423
10	149.20	937.42	96.30	0.1699	1188.266	0.68383
11	164.12	1031.16	105.93	0.1404	1080.242	0.56515
12	179.04	1124.91	115.56	0.1180	990.222	0.47488
13	193.96	1218.65	125.19	0.1005	914.051	0.40463
14	208.88	1312.39	134.82	0.0867	848.761	0.34889
15	223.80	1406.13	144.45	0.0755	792.177	0.30392

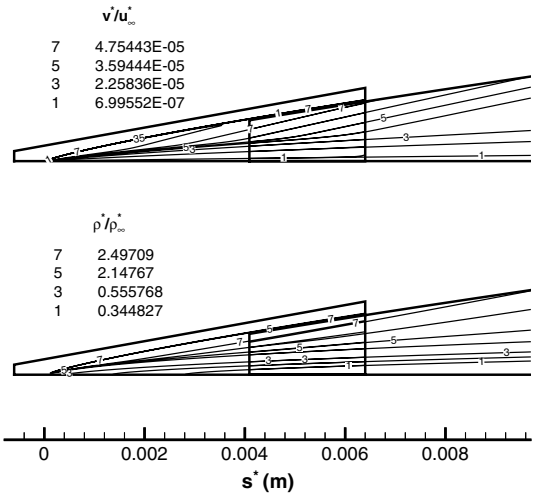

Fig. 3 Wall-normal velocity and density contours near the leading edge of the steady base flow obtained from the TVD scheme and the shock-fitting method.

IV. Results and Discussions

A. Steady Base Flow

Figure 3 shows the wall-normal velocity and density contours near the leading edge of the steady base flow obtained from the second-order TVD scheme and the fifth-order shock-fitting method. The flow including the leading edge is solved by the TVD scheme, and the flowfield after $s^* = 0.00409$ m ($R = 182.7$) is obtained from the shock-fitting method. The region from $s^* = 0.00409$ to 0.0064 m ($R = 182.7$ to 228.6) is an overlap region where the flow is computed by both methods. This figure shows that the two sets of wall-normal velocity and density contours have good agreement at the upstream boundary of the overlap region, which indicates that the solution of the TVD scheme is accurate enough to be used as an inlet condition for the fifth-order shock-fitting method in the first zone.

Figure 4 shows the pressure contour of the steady base flow obtained from the fifth-order shock-fitting method. The upper boundary of the flowfield represents the bow shock induced by the sharp wedge and the displacement thickness of the boundary layer. The lower boundary is the surface of the sharp wedge. A part of the pressure contour ranging from $x^* = 0.05$ to 0.15 m ($R = 638.9$ to 1106.7) is zoomed in to clearly show the pressure contour within the boundary layer. It is noted that pressure is approximately a constant across the boundary layer and along the Mach lines. Along a line across the flowfield in the wall-normal direction, pressure behind the shock is higher than that on the wedge surface, due to the existence of the bow shock. Figure 5 shows the pressure distribution along the wedge surface obtained from the fifth-order shock-fitting method. The theoretical inviscid limit is also plotted in the figure for

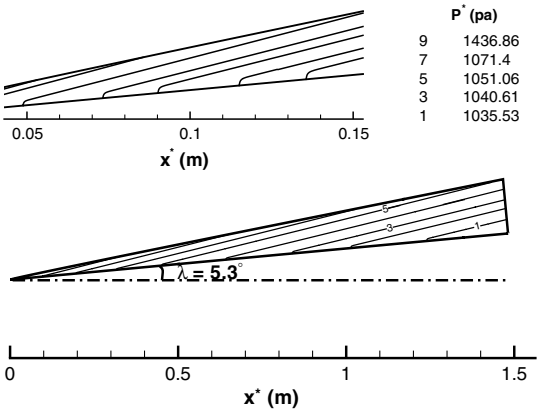

Fig. 4 Pressure contour of the steady base flow obtained from the shock-fitting method.

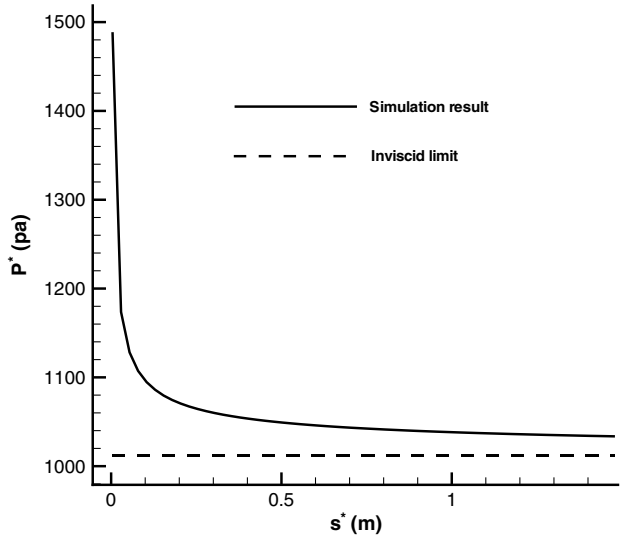

Fig. 5 Pressure distribution along the wedge surface obtained from the shock-fitting method.

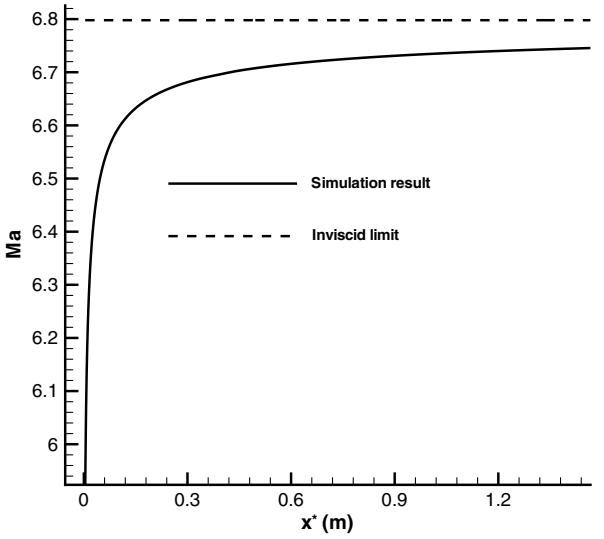

Fig. 7 Distribution of Mach number behind the bow shock obtained from the shock-fitting method.

comparison. Near the leading edge, pressure of the numerical simulation is approximately 1.5 times that of the theoretical inviscid limit. The large pressure gradient is caused by the interaction between the inviscid outer flow and the viscous boundary layer. From upstream to downstream, the viscous/inviscid interaction becomes weaker, with the bow shock moving away from the boundary layer. As a result, pressure drops quickly and approaches the constant value of the inviscid limit. However, pressure of the numerical simulation at the exit of the computational domain is still higher than that of the theoretical inviscid limit, resulting from the displacement thickness of the boundary layer.

Figure 6 shows the position and angle of the bow shock obtained from the fifth-order shock-fitting method, together with those of the theoretical inviscid limit. The solid line represents the shock front of the numerical simulation, and the dash–dotted line is a straight line representing the oblique shock induced by an inviscid flow with the same freestream conditions. The figure shows that the shock front is not a straight line, with the shock angle decreasing from 14.793° near the leading edge to 11.307° at the exit of the computational domain. In the inviscid limit, the shock angle is a constant of 11.102°. Figure 7 shows the distribution of Mach number behind the bow shock obtained from the fifth-order shock-fitting method. The theoretical inviscid limit of Mach number behind the oblique shock is also plotted in the figure for comparison. It shows that Mach number increases from 5.911 near the leading edge to 6.746 at the exit of the computational domain. For an inviscid Mach 8 flow over the 5.3° half-angle sharp wedge, the Mach number behind the shock is 6.798. Figures 6 and 7 show that the shock angle and Mach number behind the shock of the numerical simulation are quite different from those of the theoretical inviscid limit near the leading edge. Similar to pressure, large gradients of shock angle and Mach number behind the shock near the leading edge are caused by the viscous/inviscid interaction.

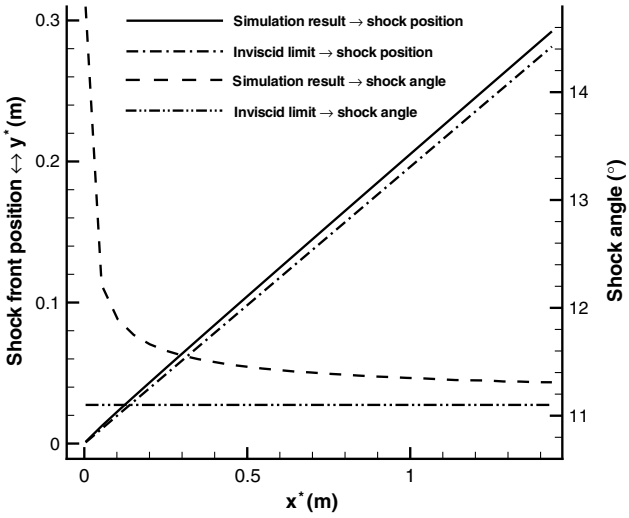

Fig. 6 Position and angle of the bow shock obtained from the shock-fitting method.

B. Stability Characteristics of Boundary-Layer Waves

Stability characteristics of boundary-layer waves of the Mach 8 flow over the sharp wedge is evaluated by the conventional LST based on the multidomain spectral method of Malik [26]. The velocity, pressure, and temperature disturbances are represented by harmonic waves of the form

$$\begin{Bmatrix} \tilde{u} \\ \tilde{v} \\ \tilde{w} \\ \tilde{p} \\ \tilde{T} \end{Bmatrix} = \begin{Bmatrix} \hat{u}(y) \\ \hat{v}(y) \\ \hat{w}(y) \\ \hat{p}(y) \\ \hat{T}(y) \end{Bmatrix} e^{i(\alpha_c x + \beta_c z - \omega_c t)} \tag{26}$$

Similar to Eq. (16), the parameters α_c and β_c are wave number components in the streamwise and spanwise directions, and ω_c is the circular frequency. For two-dimensional disturbances, $\beta_c = 0$. Substituting Eq. (26) and the steady base flow into the linearized compressible Navier–Stokes equations, an ordinary-differential-equation (ODE) system is achieved, i.e.,

$$\left(A\frac{\mathrm{d}^2}{\mathrm{d}y^2} + B\frac{\mathrm{d}}{\mathrm{d}y} + C\right)\phi = 0 \tag{27}$$

where ϕ is the disturbance vector defined by $\{\hat{u}, \hat{v}, \hat{p}, \hat{T}, \hat{w}\}$. The coefficient matrices, A, B, and C, were given in Malik's paper [26]. For spatial stability analyses, ω_c and β_c are specified real numbers, and α_c is a complex number and needs to be solved as the eigenvalue of the ODE system. The complex wave number α_c can be expressed as

$$\alpha_c = \alpha_r + i\alpha_i \tag{28}$$

where $-\alpha_i$ is the growth rate. A wave is unstable when $\alpha_i < 0$, and it is stable when $\alpha_i > 0$. The real part of the wave number, α_r, can be used to define phase velocity:

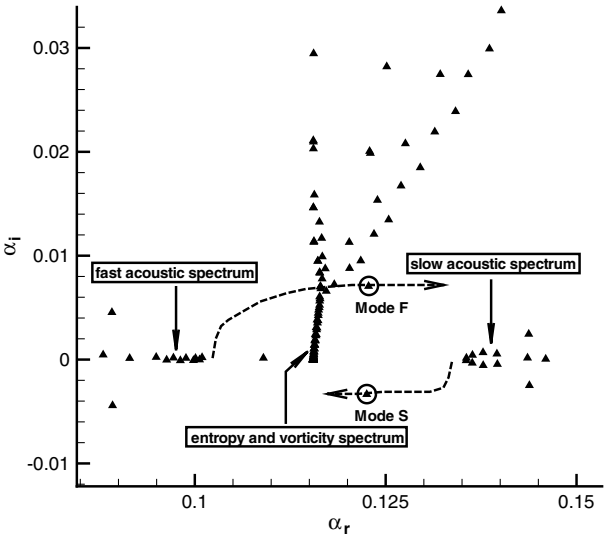

Fig. 8 Eigenvalue spectra of the ODE system for a case with the dimensionless frequency of $F = 57.78 \times 10^{-6}$ at $s^* = 0.48036$ m.

$$c = \frac{\omega_c}{\alpha_r} \tag{29}$$

Both wave number and phase velocity can be used to identify a boundary-layer wave.

Figure 8 shows an eigenvalue spectra of the ODE system for a case with the dimensionless frequency of $F = 57.78 \times 10^{-6}$ ($f^* =$ 89.52 kHz) at $s^* = 0.48036$ m ($R = 1980.44$). This frequency is the same as F_6 listed in Table 1. The figure shows the wave spectra corresponding to a fast acoustic wave, vorticity/entropy waves, and a slow acoustic wave. The two discrete modes marked by circles are mode F and mode S, originating from the fast acoustic spectrum and slow acoustic spectrum, respectively. With the frequency increasing, the real part of the wave number of mode F increases, whereas that of mode S decreases, as schematically shown in the figure by the dashed curves. The figure also shows that mode S in this case is unstable with $\alpha_i < 0$. The unstable modes at $\alpha_r = 0.09$ and 0.144 are not physical, but are numerical, resulting from the discretization of the ODE system.

Figure 9 compares the dimensionless phase velocities of mode F and mode S at three different frequencies, $f^* = 74.60$ kHz ($F =$ 48.15×10^{-6}), $f^* = 89.52$ kHz ($F = 57.78 \times 10^{-6}$), and $f^* =$ 104.44 kHz ($F = 67.41 \times 10^{-6}$), plotted as a function of the

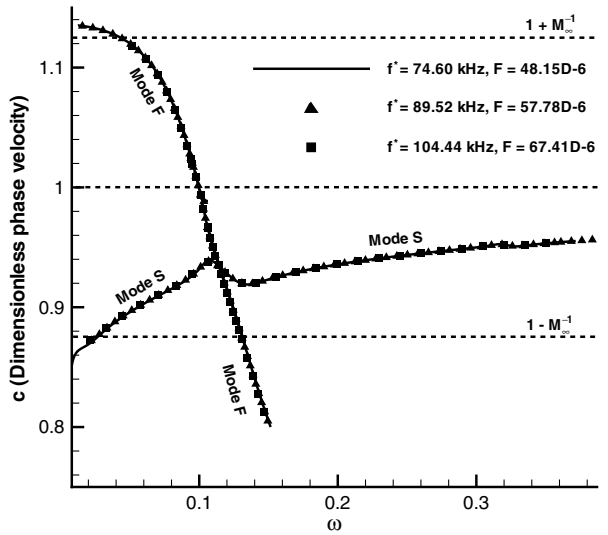

Fig. 9 Comparison of dimensionless phase velocities of mode F and mode S at three different frequencies.

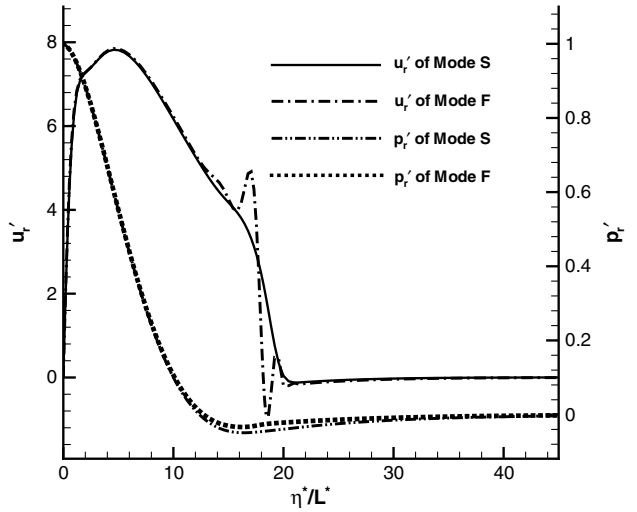

Fig. 10 Eigenfunctions of streamwise velocity and pressure of mode F and mode S at the synchronization point.

dimensionless circular frequency. According to the definition of the dimensionless circular frequency, Eq. (24), each ω corresponds to a streamwise location (s^* or R). These three frequencies are the same as F_5, F_6, and F_7 in Table 1. The three dashed lines represent the phase velocities of a fast acoustic wave ($c = 1 + M_\infty^{-1}$), vorticity/ entropy waves ($c = 1$), and a slow acoustic wave ($c = 1 - M_\infty^{-1}$), respectively. Theoretically, the phase velocities of fast and slow acoustic waves should be calculated with the Mach number behind the shock. However, Fig. 7 shows that the Mach number behind the shock is not a constant in computational domain. For convenience, the freestream Mach number is used in the current paper. The excellent agreement of phase velocities at these three frequencies indicates that the phase velocity is a function of the dimensionless circular frequency only for considered frequencies. In addition, the figure clearly shows that mode F originates from the fast acoustic wave, whereas mode S originates from slow acoustic wave. With the dimensionless circular frequency increasing, phase velocity of mode F decreases. Mode F is resonant with vorticity/entropy waves at $\omega = 0.1$. Mode S synchronizes with mode F at the point of $\omega_s = 0.11443$ and $c_s = 0.93349$. At the synchronization point, phase velocities of mode S and mode F are the same, and their eigenfunctions have a similar profile, as shown in Fig. 10. In this figure, streamwise velocity and pressure perturbations, p_r' and u_r', are normalized by the pressure perturbation on the wall. The figure shows that perturbations are confined within the boundary layer. Except the differences associated with the critical layer around $\eta^*/L^* = 19$, the eigenfunctions of mode F and mode S agree very well at the synchronization point.

For disturbances at different frequencies, the synchronization points are different in the s^* coordinate, although they have the same location with respect to dimensionless circular frequency ($\omega_s =$ 0.11443), as shown in Fig. 9. At a given dimensionless frequency, the location of the synchronization point can be calculated as

$$s_{sn}^* = \frac{(\omega_s / F_n)^2}{Re_\infty^*} \tag{30}$$

Once s_{sn}^* is known, the value of the Reynolds number at the synchronization point, R_{sn}, can be calculated using Eqs. (15) and (11).

Figure 11 compares the imaginary part of the wave number of mode F and mode S at the same set of three frequencies as a function of the dimensionless circular frequency. The vertical dashed line represents the location of the synchronization point. The horizontal dash–dotted line stands for the neutral waves ($\alpha_i = 0$). In Fig. 11, α_i of either mode S or mode F are approximately functions of the dimensionless circular frequency only. Mode S is unstable in the region from $\omega_{\mathrm{I}} = 0.04$ to $\omega_{\mathrm{II}} = 0.23$, whereas mode F is always

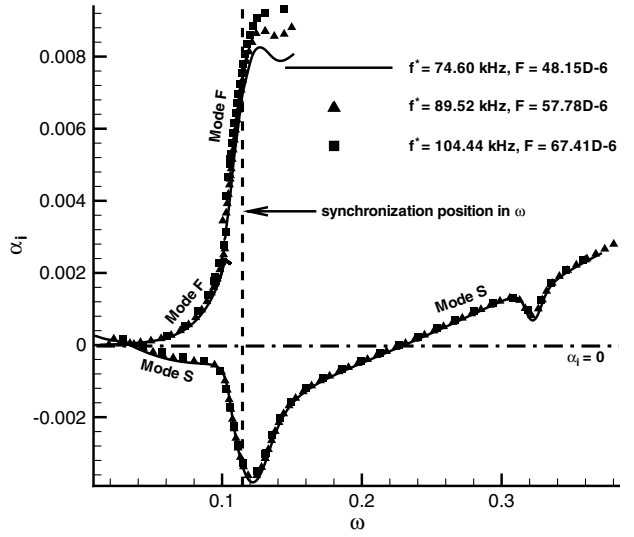

Fig. 11 Comparison of the imaginary part of the wave number of mode F and mode S at three different frequencies.

stable. It is also noted that the growth rate $(-\alpha_i)$ of mode S in the region of $\omega < 0.095$ is much smaller than that in the region of $0.1 < \omega < 0.14$, i.e., mode S is more unstable around the synchronization point.

The two parameters ω_{I} and ω_{II} define the branch I and branch II neutral points of mode S. Mode S is stable upstream of the branch I neutral point and downstream of the branch II neutral point. At a given dimensionless frequency, the location of the branch II neutral point in s^* coordinate can be calculated as

$$s^*_{\mathrm{II}n} = \frac{(\omega_{\mathrm{II}}/F_n)^2}{Re^*_\infty} \tag{31}$$

Equations (30) and (31) indicate that when the dimensionless frequency increases, the corresponding s^*_{sn} and $s^*_{\mathrm{II}n}$ decrease, i.e., the synchronization point and the branch II neutral point move upstream. Table 1 also lists locations of the synchronization point (s^*_{sn}, R_{sn}) and the branch II neutral point $(s^*_{\mathrm{II}n})$ for the 15-frequency blowing–suction disturbances. Calculations of the branch I neutral point are neglected because it is related to Mack's first mode. The current study is focused on the more unstable Mack's second mode.

C. Response to a Single-Frequency Blowing–suction Actuator

The response of the hypersonic boundary layer to an actuator at a single frequency is first studied. Wall blowing–suction at the frequency of $f^*_5 = 74.60$ kHz $(F_5 = 48.15 \times 10^{-6})$ is introduced through an actuator on the wedge surface from $s^*_i = 0.10184$ m to $s^*_e = 0.11384$ m, corresponding to $R = 911.88$ and 964,10, respectively. In this case, the blowing–suction model of Eq. (18) reduces to the following form:

$$(\rho^* v^*)' = q^*_0 \epsilon \beta(l) \sin \omega^*_5 t^* \tag{32}$$

where q^*_0 is the amplitude constant defined at the leading edge of the actuator as

Table 2 Constant q^*_0 and other parameters of the blowing–suction actuator for the seven cases of unsteady simulation

Case	q^*_0, kg/m^{2}s	s^*_i, m	s^*_e, m	s^*_c, m	R_{sc}
1	0.214139	0.05184	0.06384	0.05784	687.2
2	0.125188	0.10184	0.11384	0.10784	938.4
3	0.096130	0.15184	0.16384	0.15784	1135.2
4	0.080666	0.20184	0.21384	0.20784	1302.7
5	0.070759	0.25184	0.26384	0.25784	1450.9
6	0.063745	0.30184	0.31384	0.30784	1585.4
7	0.054453	0.40184	0.41384	0.40784	1824.8

$$q^*_0 = \rho^*_w v^*_{bk} \tag{33}$$

where ρ^*_w is the density on the wall, and v^*_{bk} is the wall-normal velocity behind the bow shock. Their values are obtained from the steady base flow. Table 2 lists parameters of the blowing–suction actuator for the seven cases of unsteady simulation considered in the current paper. The values of q^*_0 and other parameters of the single-frequency actuator considered in this section are the same as those of case 2 in Table 2.

Because of the fact that only very weak disturbances are considered, the stability simulation is in the linear region. Therefore, there should be no big difference in the results no matter which model of Eq. (16) and (18) is used to define the blowing–suction disturbance. To check that the results are essentially the same, a second blowing–suction model similar to that of Fedorov and Khokhlov [5] is tested, i.e.,

$$v^{*\prime} = v^*_{bk} \epsilon \beta(l) \sin \omega^*_5 t^* \tag{34}$$

Again, v^*_{bk} is the wall-normal velocity after the bow shock at the leading edge of the actuator, obtained from the steady base flow. Equations (32) and (34) ensure that the two models introduce the same scale of wall-normal velocity disturbances in the forcing region.

Figure 12 compares pressure perturbation amplitudes along the wedge surface for the two blowing–suction models of Eqs. (32) and (34). The good agreement between pressure perturbation amplitudes indicates that the two models are equivalent under the given conditions. This figure also shows that wall blowing–suction leads to a substantial growth of the pressure perturbation. Comparison of pressure perturbation amplitudes in the region just downstream of the actuator is shown in Fig. 13. The figure shows that there are strong modulations of pressure perturbation amplitude just downstream of the forcing region. After the location of $s^* \approx 0.56$ m $(R = 2138.3)$, the pressure perturbation increases monotonically. This location corresponds to $\omega = 0.1$.

Figure 14 shows the instantaneous pressure perturbation along the wedge surface excited by the single-frequency actuator. The amplification of the pressure perturbation from upstream to downstream indicates the excitation of unstable waves in the boundary layer. It is very likely that mode S is the unstable wave excited in the boundary layer, because mode S is more unstable in the region of 0.56 m $< s^* < 1.04$ m, corresponding to $0.1 < \omega < 0.14$, as shown in Fig. 11.

To check the properties of the unstable waves, a Fourier transform is applied to the instantaneous pressure perturbation (periodic in time) along the wedge surface, which leads to

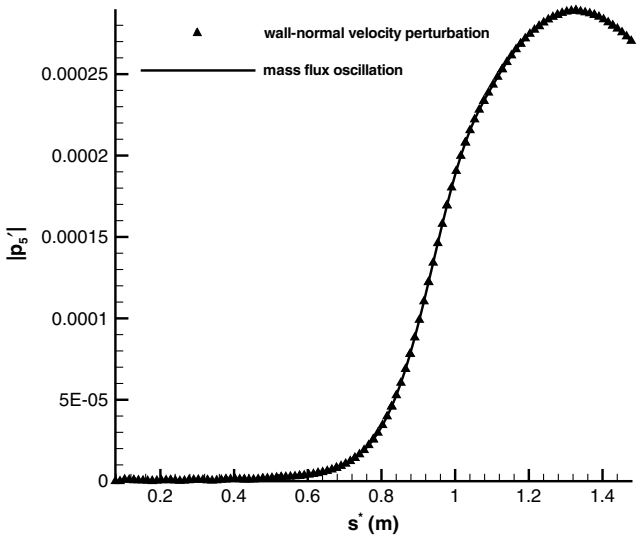

Fig. 12 Comparison of pressure perturbation amplitudes along the wedge surface for two blowing–suction models.

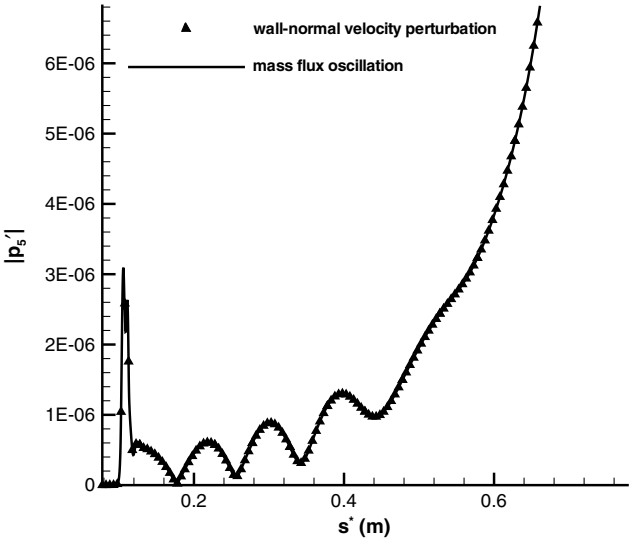

Fig. 13 Comparison of pressure perturbation amplitudes along the wedge surface in the region just downstream of the actuator.

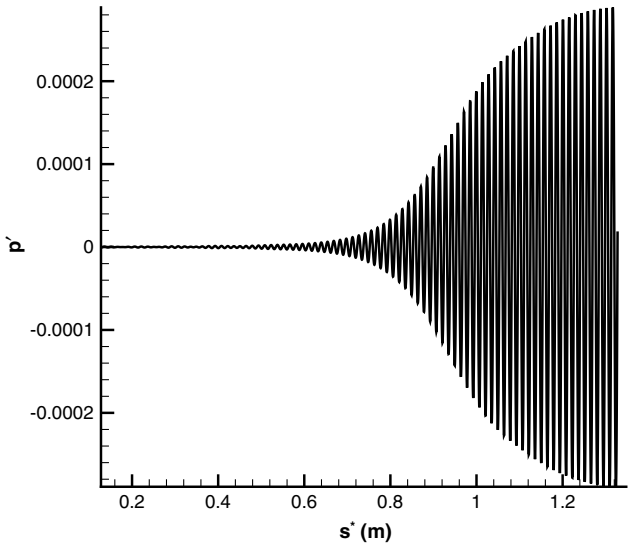

Fig. 14 Instantaneous pressure perturbation along the wedge surface excited by the single-frequency blowing–suction actuator.

$$p'(s^*, t^*) = \Sigma |p'_n(s^*)| e^{i[\phi'_n(s^*) - \omega_n^* t^*]} \tag{35}$$

where $p'(s^*, t^*)$ is the instantaneous pressure perturbation along the wedge surface. In the above equation, $|p'_n(s^*)|$ and $\phi'_n(s^*)$ are pressure perturbation amplitude and phase angle, respectively. Once $|p'_n(s^*)|$ and $\phi'_n(s^*)$ are known, the local wave number can be defined as

$$\alpha_{rn} = L^* \frac{\mathrm{d}\phi'_n}{\mathrm{d}s^*} \tag{36}$$

$$\alpha_{in} = -\frac{L^*}{|p'_n|} \frac{\mathrm{d}|p'_n|}{\mathrm{d}s^*} \tag{37}$$

where L^* is the length scale of the local boundary-layer thickness as defined by Eq. (14). The parameters α_{rn} and α_{in} will represent the true wave number only if the pressure perturbation is dominated by a single wave. Otherwise, the pressure perturbation needs to be further decomposed in order to check the properties of a specific wave. For example, Tumin et al. [7] decomposed the pressure perturbation at a location just downstream of the actuator with a biorthogonal eigenfunction system, where mode F, mode S, acoustic waves, and entropy/vorticity waves coexisted and none of them was dominant.

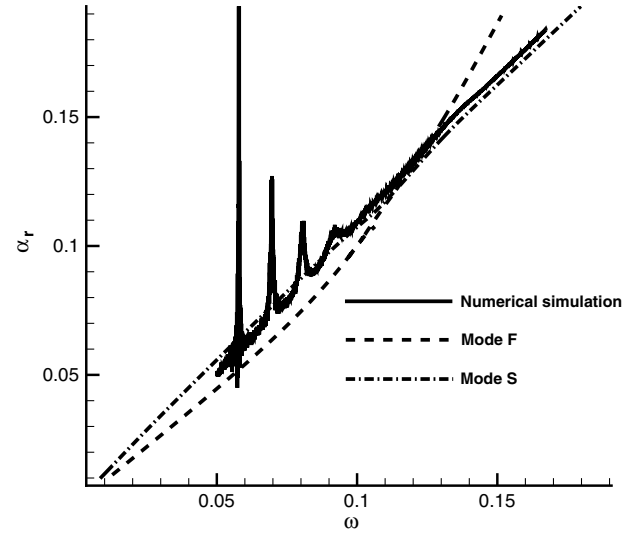

Fig. 15 Comparison of the real part of the wave number obtained from numerical simulation with those of mode F and mode S.

According to the theoretical analyses of Tumin et al. [7], the strong modulations of the pressure perturbation just downstream of the actuator, as shown in Fig. 13, result from the coexistence of mode F, mode S, acoustic waves, and entropy/vorticity waves in the boundary layer. After $s^* \approx 0.56$ m, part of the acoustic waves radiate into the flow outside the boundary layer. Mode F decays because of its inherent stability, whereas mode S grows because of its instability. Mode S eventually becomes the dominant wave in the boundary layer. Therefore, the pressure perturbations increase monotonically downstream of $s^* \approx 0.56$ m, as shown in Fig. 12.

Since our focus is on the numerical simulation results, we mainly consider the later stage, where mode S is the dominant wave in the boundary layer. In this case, Eqs. (36) and (37) can be used to evaluate the properties of the unstable mode S. Figures 15 and 16 compare the local wave number obtained from numerical simulation with those of mode F and mode S obtained from LST. These two figures show that wave number obtained from the numerical results agrees well with those of mode S after the location around $\omega = 0.1$ ($s^* = 0.56$ m). As shown in Fig. 11, this is the location where the growth rate ($-\alpha_i$) of mode S increases significantly and mode S starts

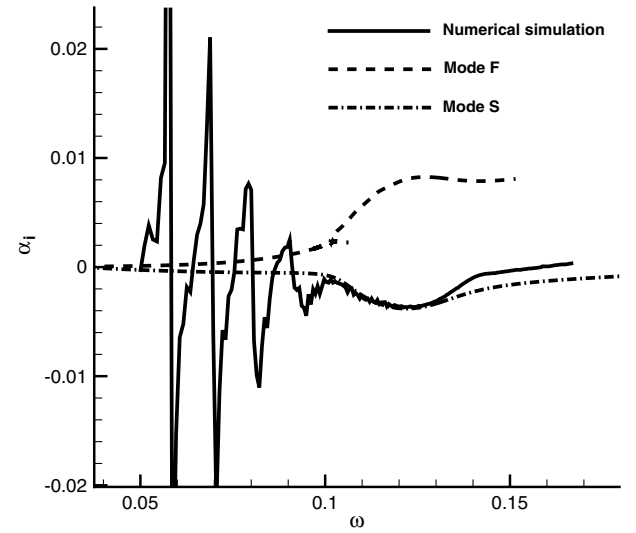

Fig. 16 Comparison of the imaginary part of the wave number obtained from numerical simulation with those of mode F and mode S.

growing to the dominant wave in the boundary layer. The results indicate that the unstable wave excited by wall blowing–suction is mode S. Figure 16 shows that the two sets of the imaginary part of the wave number agree very well in the region from $\omega = 0.1$ to 0.131. When the dimensionless circular frequency is larger than 0.131, the growth rate $(-\alpha_i)$ obtained from numerical simulation is smaller than that obtained from LST, which means that mode S obtained from numerical simulation becomes more stable than that predicted by LST. The discrepancy is caused by the nonparallel flow effects, which had been theoretically interpreted by Wang et al. [27] and Tumin et al. [28].

Figure 17 compares the eigenfunctions of mode F and mode S with the pressure perturbation obtained from numerical simulation at four different locations. Figure 17a shows that the pressure perturbation is not confined within the boundary layer, and it is quite different from the eigenfunctions of mode F and mode S. These characteristics of the pressure perturbation are caused by the coexistence of mode F, mode S, acoustic waves, and entropy/vorticity waves in the boundary layer just downstream of the blowing–suction region. Acoustic waves and entropy/vorticity waves are nonzero outside the boundary layer. Figure 17b shows that the pressure perturbation is much closer to the eigenfunction of mode S, and it is mostly confined within the

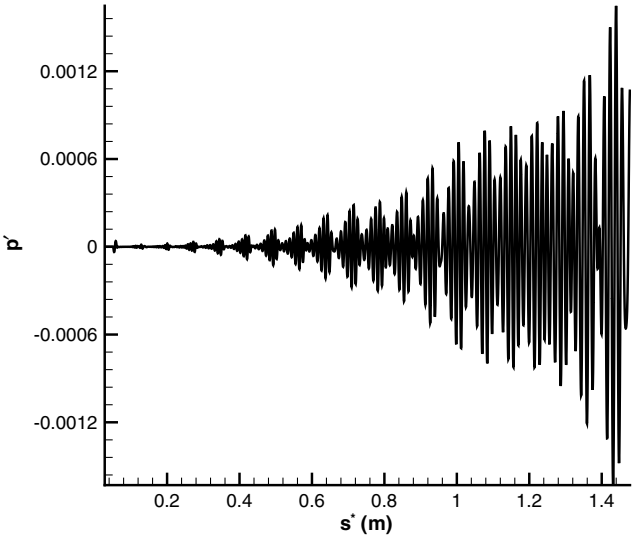

Fig. 18 Instantaneous pressure perturbation along the wedge surface excited by the 15-frequency blowing–suction actuator.

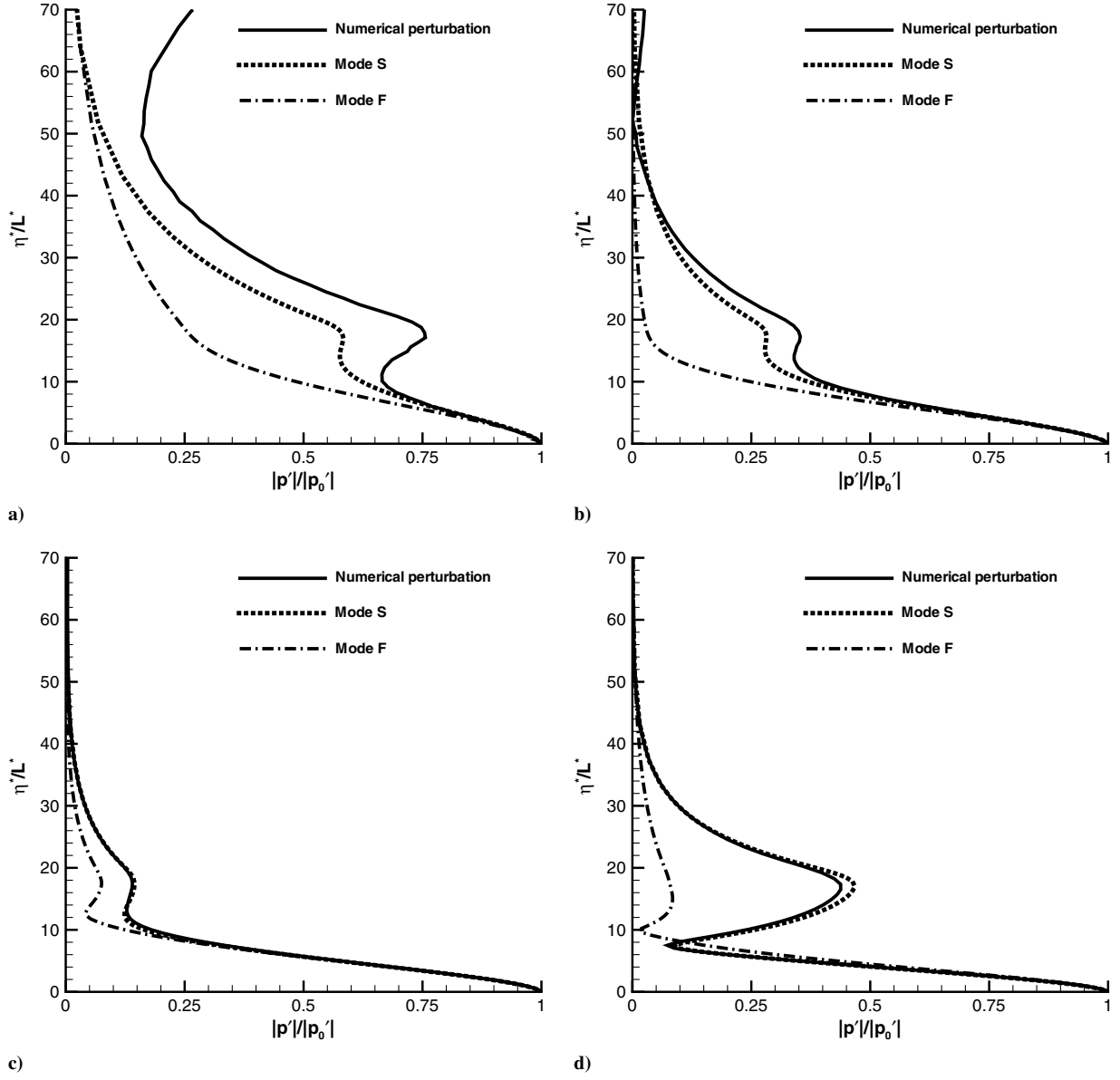

Fig. 17 Comparisons of the eigenfunctions of mode F and mode S with the pressure perturbation obtained from numerical simulation: a) $s^* = 0.26534$ m, b) $s^* = 0.46534$ m, c) $s^* = 0.66534$ m, and d) $s^* = 1.11534$ m.

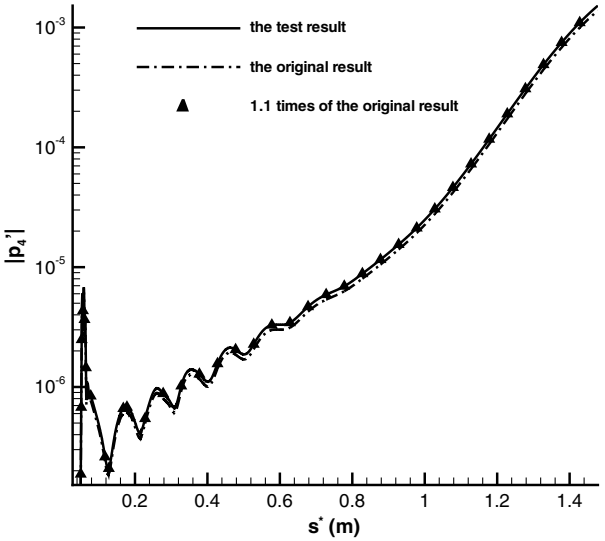

Fig. 19 Linearity test result for the pressure perturbation at the frequency f_4^*, together with the original result.

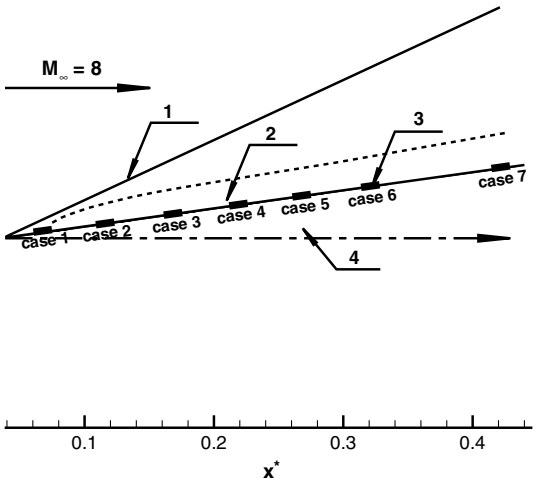

Fig. 21 Schematic of the actuator locations for the seven cases of unsteady simulation; 1: bow shock, 2: boundary layer, 3: blowing–suction actuator, and 4: sharp wedge.

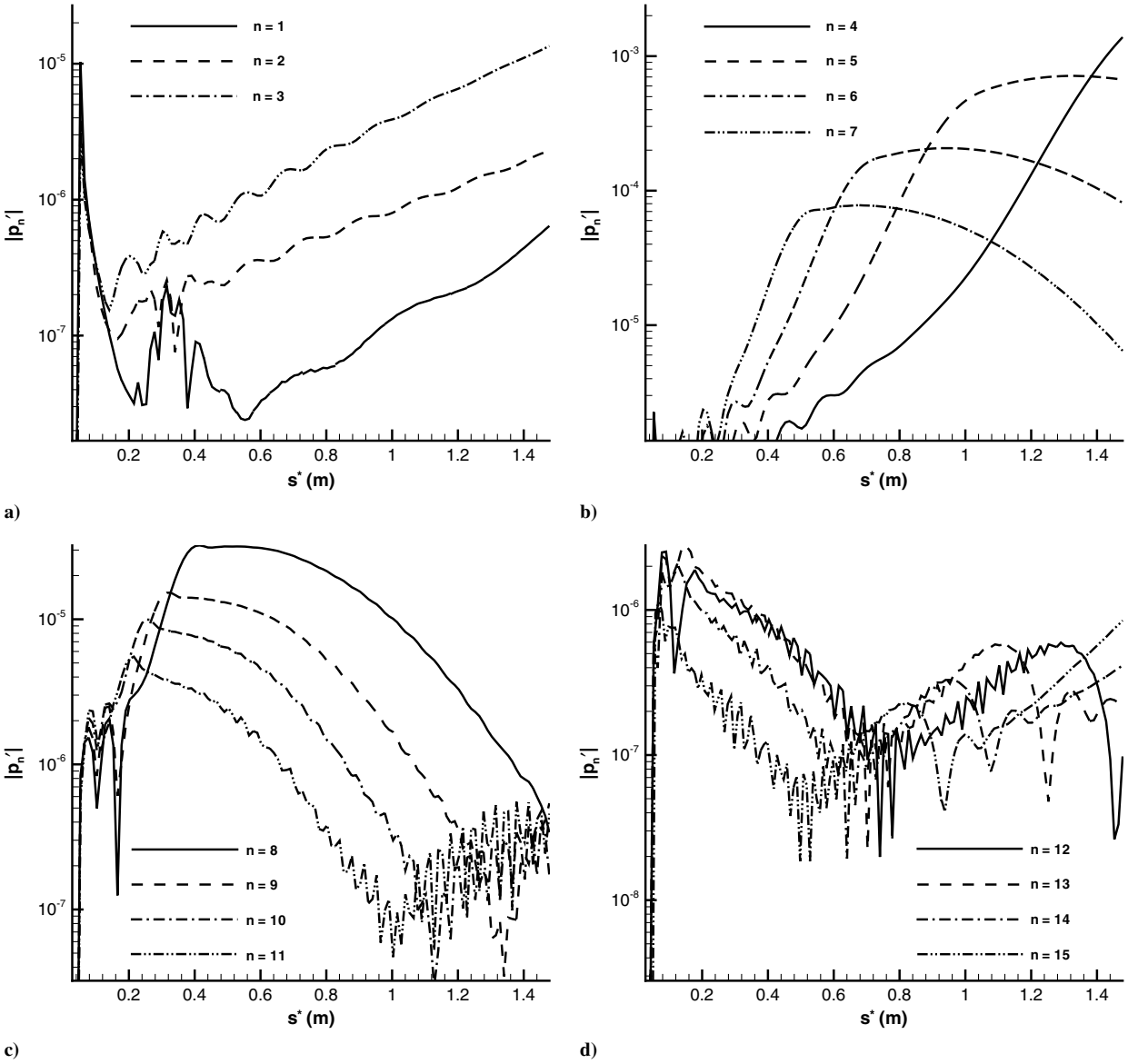

Fig. 20 Pressure perturbation amplitudes along the wedge surface excited by the 15-frequency blowing–suction actuator.

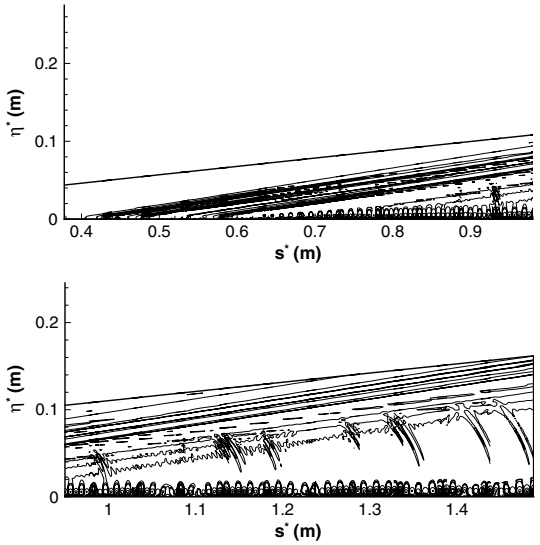

Fig. 22 Contours of the instantaneous pressure perturbation at the frequency of $f_5^* = 74.60$ kHz induced by the actuator in case 7.

Table 3 Location of the blowing–suction actuator with respect to the synchronization point for the seven cases of unsteady simulation

Case	$s_c^* < s_{sn}^*$	$s_c^* > s_{sn}^*$
1	n from 1 to 15	None
2	n from 1 to 12	n from 13 to 15
3	n from 1 to 10	n from 11 to 15
4	n from 1 to 9	n from 10 to 15
5	n from 1 to 8	n from 9 to 15
6	n from 1 to 7	n from 8 to 15
7	n from 1 to 6	n from 7 to 15

boundary layer. These characteristics of the pressure perturbation indicate that mode S becomes the dominant wave in the local boundary layer with part of the acoustic waves radiating into the flow outside the boundary layer and mode F decaying because of its inherent stability. Figures 17c and 17d show good agreement between the eigenfunction of mode S and the pressure perturbation obtained from numerical simulation, because mode S is the dominant wave in the local boundary layer downstream of the location $s^* \approx 0.56$ m.

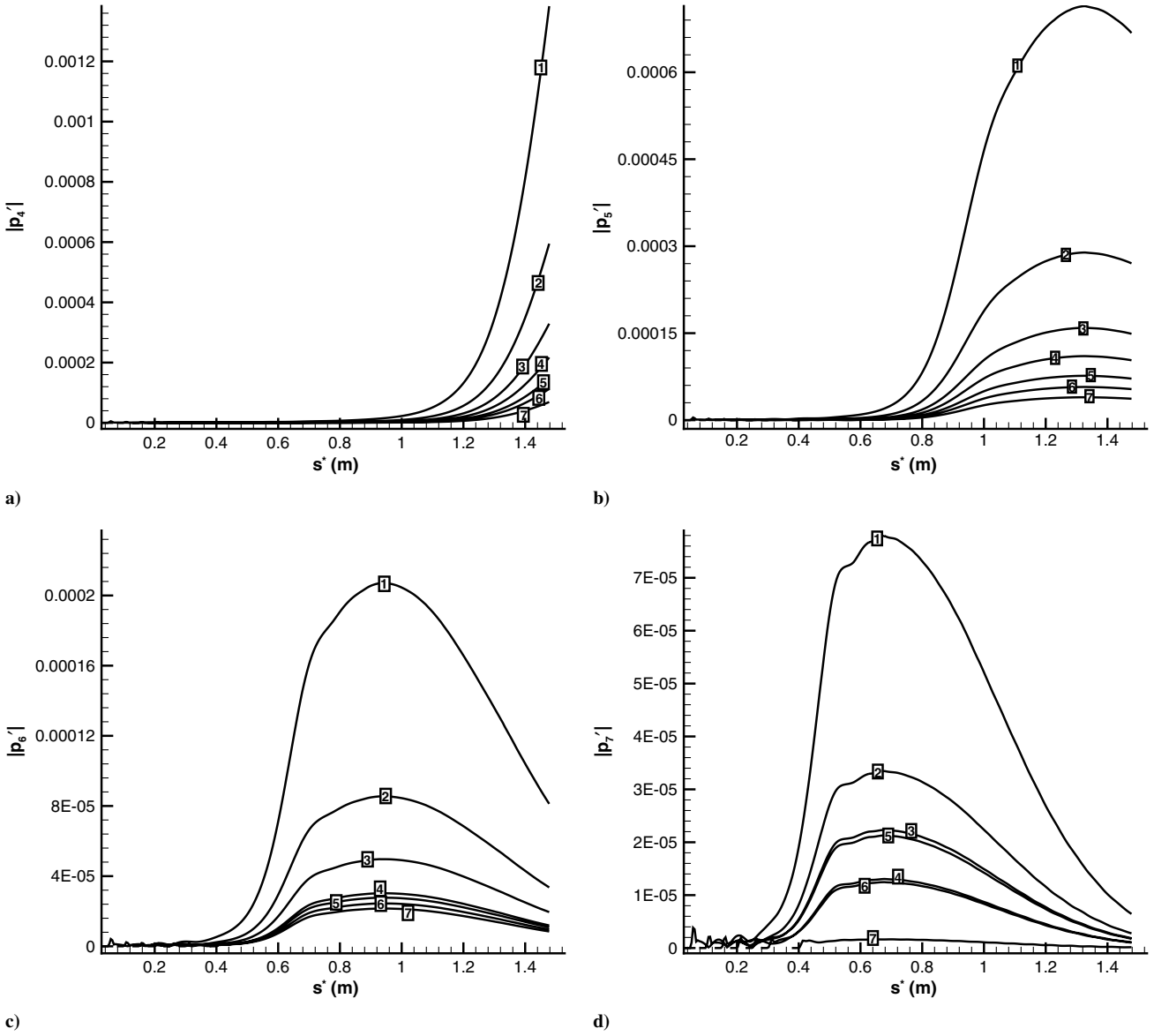

Fig. 23 Pressure perturbations at the same frequency for the seven cases of unsteady simulation: a) $f_4^* = 59.68$ kHz, b) $f_5^* = 74.60$ kHz, c) $f_6^* = 89.52$ kHz, and d) $f_7^* = 104.44$ kHz.

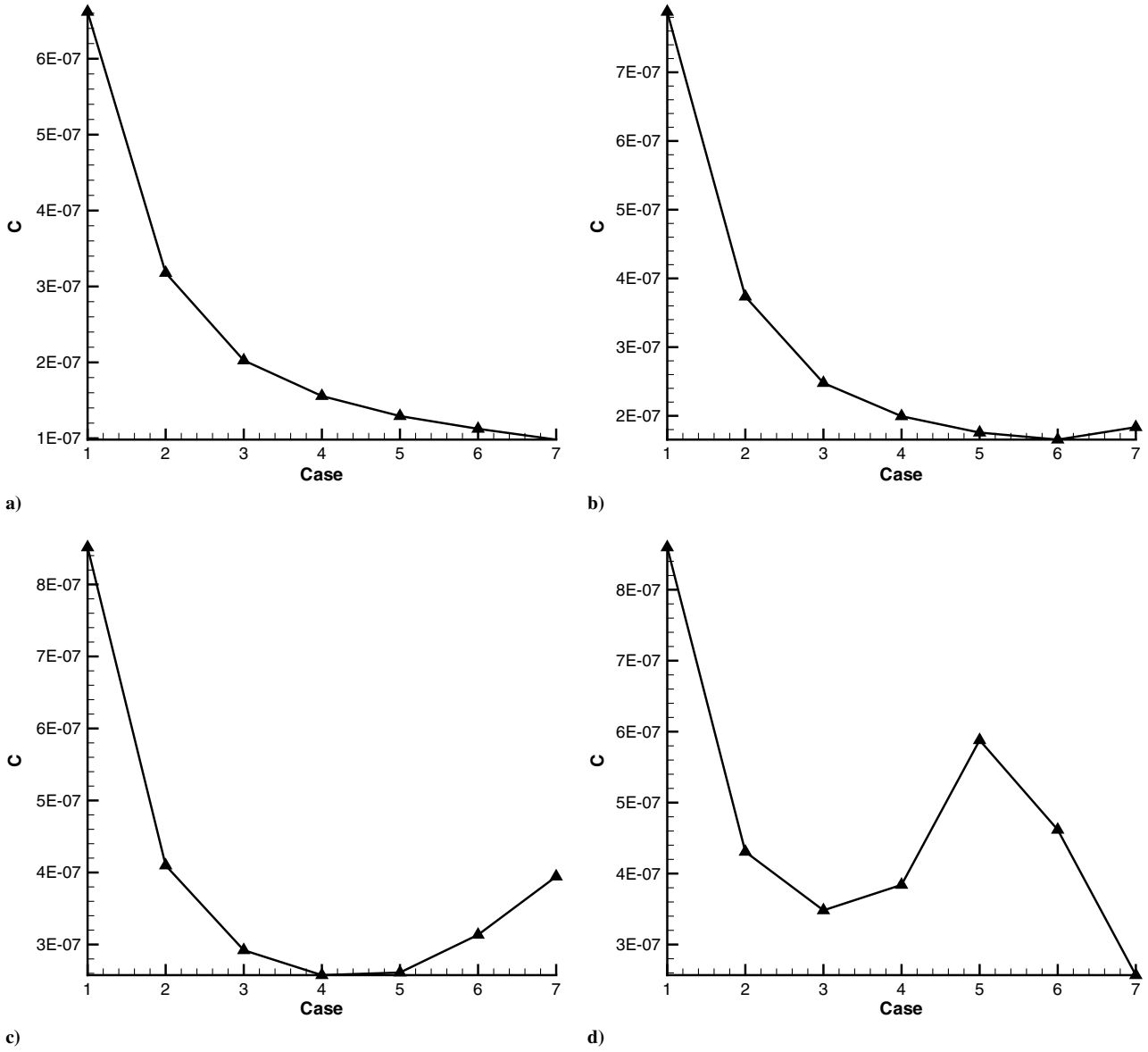

Fig. 24 Receptivity coefficients of mode S at the same frequency for the seven cases of unsteady simulation [7]: a) $f_4^* = 59.68$ kHz, b) $f_5^* = 74.60$ kHz, c) $f_6^* = 89.52$ kHz, and d) $f_7^* = 104.44$ kHz.

D. Response to a Fifteen-Frequency Blowing–suction Actuator

In this section, the response of the hypersonic boundary layer to a 15-frequency actuator is studied. Wall blowing–suction is introduced in a region on the wedge surface from $s_i^* = 0.05184$ m to $s_e^* = 0.06384$ m, corresponding to $R = 650.59$ and 721.98. The 15 frequencies f_n^* ($n = 1, 2, \ldots, 15$) are listed in Table 1. The model of the 15-frequency actuator is given by Eq. (18). The other parameters of the actuator are the same as those of case 1 in Table 2.

Figure 18 shows the instantaneous pressure perturbation along the wedge surface excited by the 15-frequency actuator. Compared with the pressure perturbation excited by a single-frequency actuator, as shown in Fig. 14, the pressure perturbation in Fig. 18 has a larger amplitude due to the coexistence of 15 pressure perturbations. The standing wave structures are the resulted of the modulations of pressure perturbations at different frequencies. Amplification of the pressure perturbation from upstream to downstream indicates the excitation of the unstable mode S. To investigate the effect of the frequency, a Fourier transform is applied to decompose the instantaneous pressure perturbation.

To check the linearity of the numerical results, a test case is computed, where the initial amplitude of the pressure perturbation at the frequency f_4^* is increased to 1.1 times the original value. Figure 19 shows the result of the test case, together with the original result. In the figure, the dash–dotted line represents the original result, the delta symbol represents 1.1 times the original result, and the solid line represents the test result. The good agreement between the test result and 1.1 times the original result indicates that the linearity of pressure perturbation still holds when its peak amplitude reaches 10^{-3}.

Figure 20 shows the pressure perturbation amplitudes along the wedge surface excited by the 15-frequency actuator. The spatial developments of pressure perturbations at different frequencies are quite different. As shown in Fig. 20a, pressure perturbations at frequencies f_1^*, f_2^*, and f_3^* grow slowly from upstream to downstream, because mode S is slightly unstable in the region of $\omega <$ 0.095. At these three frequencies, the s^* coordinates corresponding to $\omega = 0.095$ are 11.92, 2.98, and 1.32 m, respectively. In Figs. 20b and 20c , pressure perturbations at frequencies f_n^* (n from 4 to 11) grow significantly downstream of the blowing–suction region, because mode S is more unstable in the region of $0.1 < \omega < 0.14$. Just downstream of the actuator, the coexistence of mode F, mode S, acoustic waves, and entropy/vorticity waves in the boundary layer makes the growths of unstable mode S smeared. Pressure perturbations at even higher frequencies shown in Fig. 20d grow only in a small region downstream of the actuator, because the corresponding branch II neutral points of mode S are very close to the trailing edge

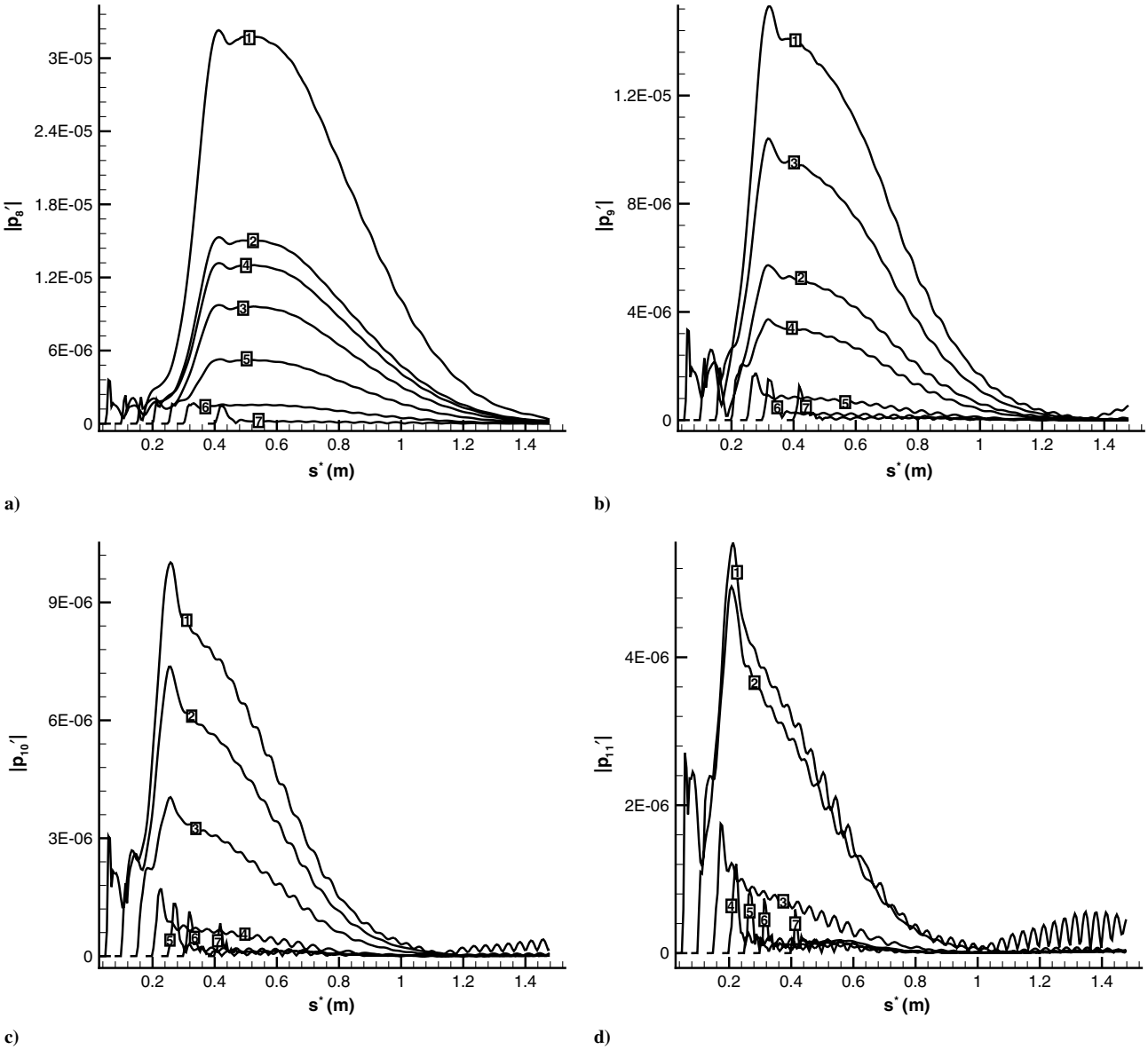

Fig. 25 Pressure perturbations at the same frequency for the seven cases of unsteady simulation: a) $f_8^* = 119.36$ kHz, b) $f_9^* = 134.28$ kHz, c) $f_{10}^* = 149.20$ kHz, and d) $f_{11}^* = 164.12$ kHz.

of the actuator. The peak amplitude of the pressure perturbation at these four frequencies after $s^* = 0.8$ m is approximately located at $\omega = 0.37$. Figure 11 shows that Mack's third mode appears at around $\omega = 0.32$. Therefore, the amplitude peak after $s^* = 0.8$ m, as shown in Fig. 20d, is not relevant to mode S.

For the pressure perturbations shown in Figs. 20b–20d , the synchronization point is within the computational domain. Figure 20 shows that the pressure perturbation starts to grow substantially at a location around the corresponding synchronization point, because mode S is more unstable in the region of $0.1 < \omega < 0.14$. However, the pressure perturbations at frequencies f_n^* $(n > 4)$ start to decrease far before reaching the corresponding branch II neutral points predicted by LST, which is caused by the nonparallel flow effects. Wang et al. [27] and Tumin et al. [28] found that nonparallel flow effect stabilizes Mack's second mode, whereas it destabilizes Mack's first mode.

E. Effect of the Actuator Location

To investigate the effect of the actuator location, seven cases of unsteady simulation are considered with the actuator shifting along the wedge surface. Figure 21 shows a schematic of the actuator locations for the seven cases of unsteady simulation. In each case, blowing–suction disturbances at 15 frequencies are introduced. The model of the actuator is given by Eq. (18). The amplitude constant q_0^* in Eq. (18) is different for the seven cases, because it is locally defined at the leading edge of the actuator. The location of the actuator is defined as

$$s_c^* = \frac{s_i^* + s_e^*}{2} \tag{38}$$

Once s_c^* is known, the value of the Reynolds number at the center of the actuator, R_{sc}, can be calculated using Eqs. (15) and (11). The amplitude constant q_0^* and other parameters of the blowing–suction actuators for the seven cases of unsteady simulation are listed in Table 2. As has been mentioned, q_0^* is defined as the product of the density on the wall and wall-normal velocity after the bow shock, with the dimension of $\mathrm{kg/m^2 s}$.

Figure 22 shows contours of the instantaneous pressure perturbation at the frequency of $f_5^* = 74.60$ kHz induced by the actuator in case 7. Downstream of the actuator, the excited pressure perturbations are divided into two branches. One branch radiates into the flow outside the boundary layer and propagates along the Mach lines (acoustic waves). The other branch stays within the boundary layer (mode F and mode S). Far downstream of the forcing region,

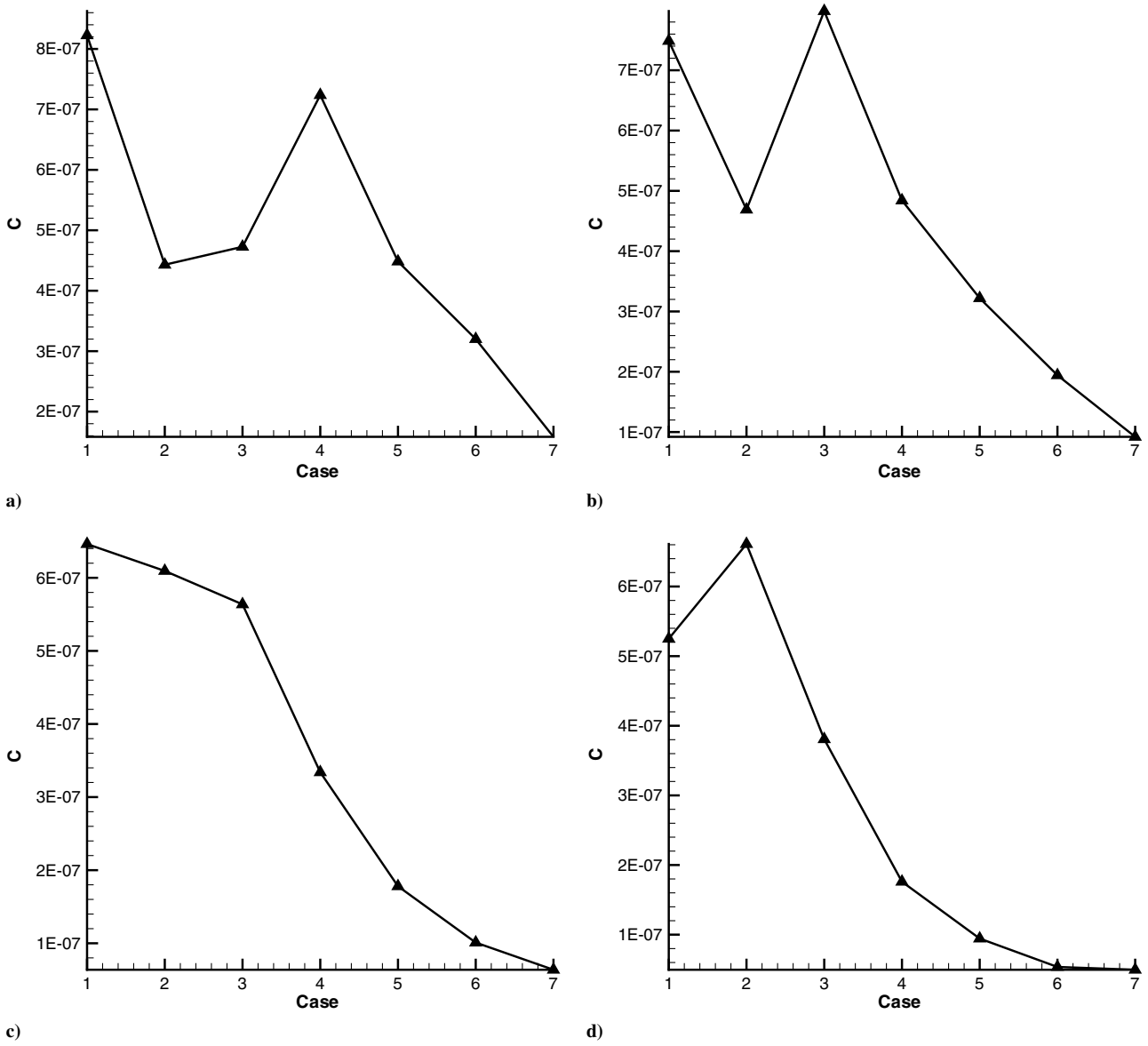

Fig. 26 Receptivity coefficients of mode S at the same frequency for the seven cases of unsteady simulation [7]: a) $f_8^* = 119.36$ kHz, b) $f_9^* = 134.28$ kHz, c) $f_{10}^* = 149.20$ kHz, and d) $f_{11}^* = 164.12$ kHz.

mode F decays because of its inherent stability, whereas mode S grows substantially because of its instability. As a result, mode S becomes the dominant wave in the boundary layer. The wave structure in the boundary layer is typical of mode S for the hypersonic boundary layer.

According to Fig. 9, the synchronization point between mode F and mode S has a dimensionless circular frequency of $\omega_s = 0.11443$. Although the synchronization point in ω coordinate does not depend on the frequency, its locations in s^* and R coordinates depend on the frequency. The s^* and R coordinates of the synchronization point at the 15 frequencies are calculated by Eqs. (30) and (15) and tabulated in Table 1 as s_{sn}^* and R_{sn}.

Table 1 shows that the synchronization point moves upstream with the frequency increasing. Therefore, the actuators for the seven cases are located either upstream or downstream of the synchronization points at different frequencies. Table 3 lists the location of the blowing–suction actuator with respect to the synchronization point for the seven cases of unsteady simulation. In this table, $s_c^* < s_{sn}^*$ and $s_c^* > s_{sn}^*$ represent that the actuator is located upstream and downstream of the synchronization point at the frequency f_n^*, respectively. For example, at the frequency of $f_5^* = 74.60$ kHz, locations of the actuators in all cases are upstream of the synchronization point. While at the frequency of $f_{10}^* = 149.20$ kHz, locations of the actuator in cases 1 to 3 are upstream of the synchronization point, whereas locations of the actuator in other cases are downstream of the synchronization point.

To show the effect of the actuator location more efficiently, pressure perturbations at the same frequency are plotted together for the seven cases of unsteady simulation. Figure 23 shows the pressure perturbations at the frequencies from f_4^* to f_7^*. Pressure perturbations at the frequencies f_1^*, f_2^*, and f_3^* are neglected, because mode S is slightly unstable in the region of $\omega < 0.095$ and the corresponding synchronization points are located downstream of the computational domain. In these figures, the numbers 1 to 7 stand for the case number. The spatial development of pressure perturbation from upstream to downstream represents a mixture of the receptivity and the downstream amplification. To separate out one mechanism from another, receptivity coefficients C of mode S obtained from Tumin et al.'s [7] paper are replotted in Fig. 24, for example, where C is defined as the initial amplitude of mode S excited by wall blowing–suction. These receptivity coefficients are helpful to qualitatively interpret numerical results.

At the frequency of $f_4^* = 59.68$ kHz, the actuators in all seven cases are located upstream of the synchronization point at $s_{s4}^* =$ 1.0618 m. Figure 23a shows that mode S is strongly excited for all seven cases. Furthermore, the amplitudes of pressure perturbations

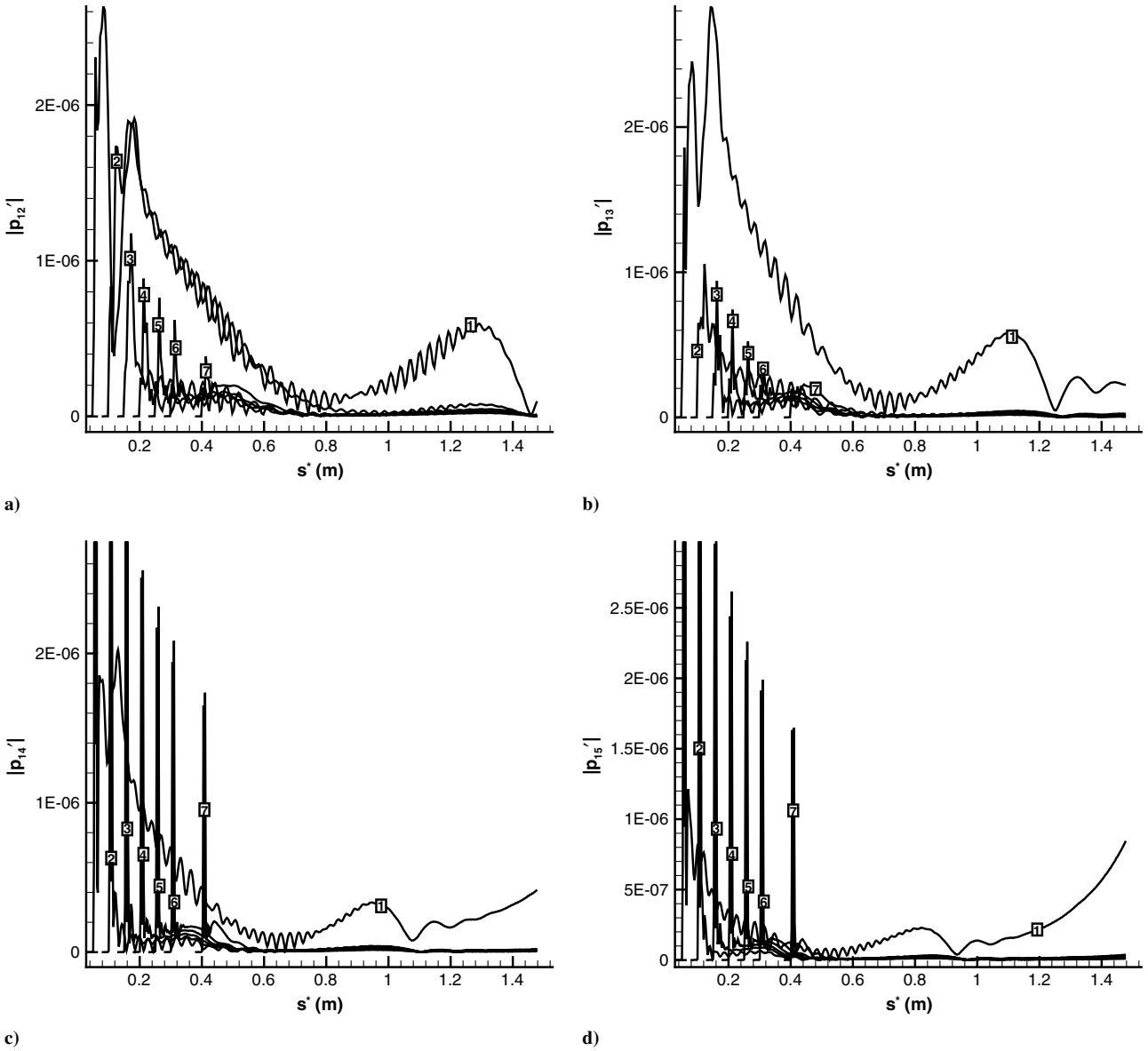

Fig. 27 Pressure perturbations at the same frequency for the seven cases of unsteady simulation: a) $f_{12}^* = 179.04$ kHz, b) $f_{13}^* = 193.96$ kHz, c) $f_{14}^* = 208.88$ kHz, and d) $f_{15}^* = 223.80$ kHz.

decrease when the actuator shifts from upstream to downstream, which is consistent with the decrease of receptivity coefficients (Fig. 24a) and the shrinkage of the amplification region. Figures 23b and 23c show similar results for the pressure perturbations at the frequencies of $f_5^* = 74.60$ kHz and $f_6^* = 89.52$ kHz, respectively. At these two frequencies, Table 3 show that the actuators in all seven cases are upstream of the corresponding synchronization points. Although receptivity coefficients at these two frequencies do not consistently decrease, as shown in Figs. 24b and 24c, the shrinkage of the amplification region makes pressure perturbation amplitude decrease, with the actuator shifting from upstream to downstream.

At the frequency of $f_7^* = 104.44$ kHz, the actuator is upstream of the synchronization point at $s_{s7}^* = 0.3467$ m in cases 1 to 6, whereas it is downstream of the synchronization point in case 7. Figure 23d shows that mode S is strongly excited in cases 1 to 6. In case 7, no exponential growth of pressure perturbation is observed. There is no significant amplification of pressure perturbation downstream of the actuator, despite the fact that the actuator is still located within the unstable region of mode S, with the corresponding branch II neutral point being at $s^* = 1.39557$ m. Figure 24d shows that the receptivity coefficient of case 7 is comparable with those of other cases. The only difference of case 7 is that the actuator is downstream of the synchronization point. It is also noted that a second peak of receptivity coefficient exists in case 5. Because of the jump of receptivity coefficient, pressure perturbation amplitude in case 5 is larger than that in case 4, despite the shrinkage of the amplification region.

At the frequency of $f_8^* = 119.36$ kHz, Fig. 25a shows that mode S is strongly excited in cases 1 to 5, while no exponential growth of pressure perturbation is observed downstream of the actuator in case 6 and case 7. Again, this is related to the fact that the actuators in cases 1 to 5 are upstream of the synchronization point at $s_{s8}^* = 0.2654$ m, whereas the actuators are located downstream of the synchronization point in case 6 and case 7. It needs to be emphasized that the actuators are still located within the unstable region of mode S, even in cases 6 and 7. Figure 26a shows that receptivity coefficients of cases 6 and 7 are comparable with those of the other five cases. A second peak of receptivity coefficient exists in case 4. The jump of receptivity coefficient leads to a larger amplitude of pressure perturbation in case 4 than that in case 3.

As the frequency changes to $f_9^* = 134.28$ kHz in Fig. 25b, the actuators are located upstream of the synchronization point at $s_{s9}^* = 0.2097$ m in cases 1 to 4, whereas the actuator in cases 5 to 7 are downstream of the synchronization point. The results at this frequency are consistent with those of the previous frequencies regarding the excitation of mode S. Mode S is strongly excited in cases 1 to 4. However, there is no significant amplification of pressure

perturbation downstream of the actuator in cases 5 to 7. Figure 26b shows that receptivity coefficients of cases 5 to 7 are comparable with those of the other four cases. It also shows a second peak of receptivity coefficient exists in case 3, which leads to a larger amplitude of pressure perturbation in case 3 than that in case 2.

At the frequencies of f_n^* with n from 10 to 11, a similar conclusion can be drawn. In cases in which the actuator is downstream of the synchronization point, no exponential growth of pressure perturbation is observed, despite the facts that the actuators are still located within the unstable region of mode S and receptivity coefficients are comparable with those of the cases in which the actuator is upstream of the synchronization point (Figs. 26c and 26d). For even higher frequencies, Fig. 27 shows that the pressure perturbation grows in a very small region downstream of the actuator, because the unstable region of mode S is small. As has been mentioned, the peak amplitude of the pressure perturbation at these four frequencies after $s^* = 0.8$ m is not relevant to mode S.

Figures 23, 25, and 27 consistently show that mode S at a specific frequency is strongly excited when the actuator is located upstream of the corresponding synchronization point. When the actuator is downstream of the synchronization point, no significant amplification of pressure perturbation is observed downstream of the actuator. This result represents a mixture of the receptivity and the downstream growth of mode S. The exact cause and mechanism of this result is not clear. However, such a result is observed for wall blowing–suction at all frequencies considered in the current study. To excite strong mode S at a specific frequency, the result indicates that it is necessary to place the blowing–suction actuator upstream of the corresponding synchronization point.

V. Conclusions

The response of a Mach 8 flow over a sharp wedge of a half-angle of 5.3° to wall blowing–suction has been studied by numerical simulation and linear stability theory. Steady base flow is obtained by solving the compressible Navier–Stokes equations with a combination of a fifth-order shock-fitting method and a second-order TVD scheme. The TVD scheme is only used to solve the steady base flow in a small region including the leading edge. Stability characteristics of the boundary-layer waves are evaluated by the linear stability theory. In stability simulations, wall blowing–suction is introduced through an actuator on the wedge. The simulation of unsteady flow is carried out using the shock-fitting method.

The response of the hypersonic boundary layer to a single-frequency blowing–suction actuator is first studied. The numerical results and LST analyses show that mode F, mode S, acoustic waves, and entropy/vorticity waves are simultaneously excited by the blowing–suction actuator. All these waves coexist in the boundary layer just downstream of the forcing region, which leads to strong modulations of the pressure perturbation. Far downstream of the forcing region, part of the acoustic waves radiate into the flow outside the boundary layer. Mode F decays because of its inherent stability, whereas mode S grows substantially because of its instability. As a result, mode S becomes the dominant wave in the boundary layer.

The response of the hypersonic boundary layer to a 15-frequency actuator is also studied. The results show that spatial developments of pressure perturbations at different frequencies are quite different, although they have the same initial amplitudes introduced by the actuator. Pressure perturbation at a specific frequency starts to decrease far before reaching the corresponding branch II neutral point predicted by LST, which is caused by the nonparallel flow effects. Mack's second mode is stabilized by the nonparallel flow effects.

Seven cases of stability simulations are considered with the actuator shifting along the wedge surface to study the effect of the actuator location. The numerical results consistently show that mode S at a specific frequency is strongly excited when the actuator is located upstream of the corresponding synchronization point. On the other hand, when the actuator is downstream of the corresponding synchronization point, there is no significant amplification of pressure perturbation downstream of the actuator. This result represents a mixture of the receptivity and the downstream growth of mode S. The exact cause and mechanism of this result are not clear. However, such a result is obtained for wall blowing–suction at all frequencies considered in the current study. To excite strong mode S at a specific frequency, the result indicates that it is necessary to place the blowing–suction actuator upstream of the corresponding synchronization point. Further theoretical analysis is needed to reveal the mechanism behind the numerical results. It is hoped that this paper can motivate further theoretical analysis.

Acknowledgments

This work was sponsored by the U.S. Air Force Office of Scientific Research (AFOSR) under grant nos. FA9550-07-1-0414 and FA9550-04-1-0029, monitored by John Schmisseur, and the AFOSR/NASA National Center for Hypersonic Research in Laminar-Turbulent Transition. The views and conclusions contained herein are those of the authors and should not be interpreted as necessarily representing the official policies or endorsements either expressed or implied, of the AFOSR or the U.S. Government.

References

[1] Reshotko, E., "Is Re_θ/Me a Meaningful Transition Criterion?," *AIAA Journal*, Vol. 45, No. 7, 2007, pp. 1441–1443. doi:10.2514/1.29952

[2] Saric, W. S., Reed, H. L., and Kerschen, E. J., "Boundary-Layer Receptivity to Freestream Disturbances," *Annual Review of Fluid Mechanics*, Vol. 34, 2002, pp. 291–319. doi:10.1146/annurev.fluid.34.082701.161921

[3] Fedorov, A. V., and Khokhlov, A. P., "Excitation of Unstable Modes in a Supersonic Boundary Layer by Acoustic Waves," *Fluid Dynamics*, Vol. 26, No. 4, 1991, pp. 531–537. doi:10.1007/BF01050314

[4] Fedorov, A. V., and Khokhlov, A. P., "Prehistory of Instability in a Hypersonic Boundary Layer," *Theoretical and Computational Fluid Dynamics*, Vol. 14, No. 6, 2001, pp. 359–375. doi:10.1007/s001620100038

[5] Fedorov, A. V., and Khokhlov, A. P., "Receptivity of Hypersonic Boundary Layer to Wall Disturbances," *Theoretical and Computational Fluid Dynamics*, Vol. 15, 2002, pp. 231–254. doi:10.1007/s001620100052

[6] Tumin, A., "Three-Dimensional Spatial Normal Modes in Compressible Boundary Layers," *Journal of Fluid Mechanics*, Vol. 586, 2007, pp. 295–322. doi:10.1017/S002211200700691X

[7] Tumin, A., Wang, X., and Zhong, X., "Direct Numerical Simulation and the Theory of Receptivity in a Hypersonic Boundary Layer," *Physics of Fluids*, Vol. 19, 2007, Paper 014101. doi:10.1063/1.2409731

[8] Maslov, A. A., and Semionov, N. V., "Excitation Of Natural Oscillations in a Boundary Layer by an External Acoustic Field," *Fluid Dynamics*, Vol. 21, 1986, pp. 400–404. doi:10.1007/BF01409724

[9] Maslov, A. A., Shiplyuk, A. N., Sidorenko, A., and Arnal, D., "Leading-Edge Receptivity of a Hypersonic Boundary Layer on a Flat Plate," *Journal of Fluid Mechanics*, Vol. 426, 2001, pp. 73–94. doi:10.1017/S0022112000002147

[10] Fedorov, A. V., "Receptivity of a High-Speed Boundary Layer to Acoustic Disturbances," *Journal of Fluid Mechanics*, Vol. 491, 2003, pp. 101–129. doi:10.1017/S0022112003005263

[11] Semionov, N. V., and Kosinov, A. D., "An Experimental Study of Receptivity of Supersonic Boundary Layer on a Blunted Plate," *International Journal of Mechanics and Control* , Vol. 2, No. 3, 2008, pp. 87–95.

[12] Wheaton, B. M., Juliano, T. J., Berridge, D. C., Chou, A., Gilbert, P. L., Casper, K. M., et al., "Instability and Transition Measurements in the Mach-6 Quiet Tunnel," AIAA Paper 2009-3559, June 2009.

[13] Malik, M. R., Lin, R. S., and Sengupta, R., "Computation of Hypersonic Boundary-Layer Response to External Disturbances," AIAA Paper 1999-0411, Jan. 1999.

[14] Zhong, X., "Leading-Edge Receptivity to Free Stream Disturbance Wave for Hypersonic Flow over a Parabola," *Journal of Fluid Mechanics*, Vol. 441, 2001, pp. 315–367.

[15] Ma, Y., and Zhong, X., "Receptivity of a Supersonic Boundary Layer over a Flat Plate. Part 2:Receptivity to Freestream Sound," *Journal of*

Fluid Mechanics, Vol. 488, 2003, pp. 79–121.
doi:10.1017/S0022112003004798

[16] Egorov, I. V., Sudakov, V. G., and Fedorov, A. V., "Numerical Modeling of the Stabilization of a Supersonic Flat-Plate Boundary Layer by a Porous Coating," *Fluid Dynamics*, Vol. 41, No. 3, 2006, pp. 356–365.
doi:10.1007/s10697-006-0051-x

[17] Egorov, I. V., Fedorov, A. V., and Sudakov, V. G., "Direct Numerical Simulation of Disturbances Generated by Periodic Suction-Blowing in a Hypersonic Boundary Layer," *Theoretical and Computational Fluid Dynamics*, Vol. 20, No. 1, 2006, pp. 41–54.
doi:10.1007/s00162-005-0001-y

[18] Zhong, X., and Ma, Y., "Boundary-Layer Receptivity of Mach 7.99 Flow over A Blunt Cone to Free-Stream Acoustic Waves," *Journal of Fluid Mechanics*, Vol. 556, 2006, pp. 55–103.
doi:10.1017/S0022112006009293

[19] Fedorov, A. V., and Khokhlov, A. P., "Excitation and Evolution of Unstable Disturbances in Supersonic Boundary Layer," *Transitional and Turbulent Compressible Flows*, edited by L. D. Kral, and T. A. Zang, Vol. 151, ASME International, New York, 1993, pp. 1–13.

[20] Maslov, A. A., Kudryavtsev, A. N., Mironov, S. G., Poplavskaya, T. V., and Tsyryulnikov, I. S., "Numerical Simulation of Receptivity of a Hypersonic Boundary Layer to Acoustic Disturbances," *Journal of Applied Mechanics and Technical Physics*, Vol. 48, No. 3, 2007, pp. 368–374.
doi:10.1007/s10808-007-0046-3

[21] Malik, M. R., and Balakumar, P., "Acoustic Receptivity of Mach 4.5 Boundary Layer with Leading-Edge Bluntness," *Theoretical and Computational Fluid Dynamics*, Vol. 21, 2007, pp. 323–342.
doi:10.1007/s00162-007-0050-5

[22] Wang, X., and Zhong, X., "Effect of Wall Perturbations on the Receptivity of a Hypersonic Boundary Layer," *Physics of Fluids*, Vol. 21, 2009, Paper 044101.
doi:10.1063/1.3103880

[23] Egorov, I. V., Fedorov, A. V., and Soudakov, V. G., "Receptivity of a Hypersonic Boundary Layer over a Flat Plate with a Porous Coating," *Journal of Fluid Mechanics*, Vol. 601, 2008, pp. 165–187.

[24] Zhong, X., "High-Order Finite-Difference Schemes for Numerical Simulation of Hypersonic Boundary-Layer Transition," *Journal of Computational Physics*, Vol. 144, 1998, pp. 662–709.
doi:10.1006/jcph.1998.6010

[25] Eibler, W., and Bestek, H., "Spatial Numerical Simulations of Linear and Weakly Nonlinear Instabilities in Supersonic Boundary Layers," *Theoretical and Computational Fluid Dynamics*, Vol. 8, 1996, pp. 219–235.
doi:10.1007/BF00418059

[26] Malik, M. R., "Numerical Methods for Hypersonic Boundary Layer Stability," *Journal of Computational Physics*, Vol. 86, 1990, pp. 376–413.
doi:10.1016/0021-9991(90)90106-B

[27] Wang, X., Tumin, A., and Zhong, X., "DNS and Theoretical Study of Perturbations in a Hypersonic Boundary Layer over a Flat Plate," *Bulletin of the American Physical Society*, Vol. 53, No. 15, 2008, p. 180.

[28] Tumin, A., Wang, X., and Zhong, X., "Numerical Simulation and Theoretical Analysis on Hypersonic Boundary-Layer Receptivity to Wall Blowing–suction," AIAA Paper 2010-0354, Jan. 2010.

A. Tumin
Associate Editor